



Comparative analysis of bent and basic winglets on performance improvement of horizontal axis wind turbines

Zhihao Zhang ^a, Limin Kuang ^{a,c}, Zhaolong Han ^{a,b,*}, Dai Zhou ^a, Yongsheng Zhao ^{a,b}, Yan Bao ^a, Lei Duan ^a, Jiahuang Tu ^d, Yaoran Chen ^e, Mingsheng Chen ^f

^a State Key Laboratory of Ocean Engineering and School of Naval Architecture, Ocean and Civil Engineering, Shanghai Jiao Tong University, Shanghai, 200240, China

^b Institute of Polar and Ocean Technology, Institute of Marine Equipment, Shanghai Jiao Tong University, Shanghai, 200240, China

^c Department of Civil Engineering, Yokohama National University, Yokohama, 240-8501, Japan

^d College of Civil Engineering, Xiangtan University, Xiangtan, 411105, China

^e Institute of Artificial Intelligence, Collaborative Innovation Center for the Marine Artificial Intelligence, Shanghai University, Shanghai, 200444, China

^f School of Naval Architecture, Ocean and Energy Power Engineering, Wuhan University of Technology, Wuhan, 430063, China

ARTICLE INFO

Handling Editor: Jesse L. The

Keywords:

Bent winglet
Horizontal axis wind turbine
Computational fluid dynamics
Platform motion

ABSTRACT

The winglet has been widely deployed in the optimization of the blade design as it reduces the tip loss of the blade and increases the swept area of the rotor. However, previous studies have not adequately investigated the effect of platform motion on winglet performance in wind turbines. The objective of this study is to propose a novel bent winglet structure for wind turbines to improve performance under both stationary and surge conditions. To achieve this, the NREL Phase VI horizontal axis wind turbine (HAWT) is treated as a baseline. The numerical method employed is validated by comparing the simulated power and pressure coefficients of the HAWT with experimental data from the literature. The performance of the conventional winglet with the proposed novel winglet is compared in detail, taking into account the cant, twist, expansion direction, length, and winglet number of the conventional winglet. The results show that the novel bent winglet exhibits superior performance, with a 14.5% improvement in performance compared to the conventional winglet under surge motion. This study provides a feasible scenario for the optimization of onshore and offshore wind turbine designs.

1. Introduction

The global energy crisis and the emission of greenhouse gases have resulted in a substantial increase in demand for alternatives to traditional chemical energy sources [1–3]. This has led to a focus on the development and utilization of clean energy sources such as solar energy, geothermal energy, ocean tidal wave energy, and wind energy. Among these, wind resources are widely distributed on the earth, with abundant wind energy available not only on land but also offshore, offering a broad prospect. In 2021, global offshore wind energy achieved a record year for deployment, with 17,398 MW of new projects commissioned [4].

Wind turbines are essential devices for capturing wind energy and they can be classified into two main categories: horizontal-axis wind turbines (HAWTs) and vertical-axis wind turbines (VAWTs).

Commercial applications of HAWTs have already been implemented and have evolved from small wind turbines (e.g., NREL Phase VI) to ultra-large wind turbines with 20 MW [5]. Small-scale HAWTs are widely employed in both onshore and offshore applications (Fig. 1). These HAWTs are appropriate for specific urban areas with relatively uniform wind directions, such as between buildings and on rooftops (Fig. 1(a)); they can also be installed in small floating offshore wind farms (Fig. 1(b)). The blade optimization for small-scale wind turbines to enhance performance has attracted the attention of some researchers [6,7].

The power efficiency of small wind turbines is generally lower than that of their larger counterparts. Therefore, improving the aerodynamic performance of HAWTs is of paramount importance [9,10]. Researchers have focused on the optimization of blades and configuration for HAWTs to enhance their power efficiency. Various measures have been investigated, such as bionic blades with leading edges tubercles [11], Gurney flap [12], cavities on the blade surface [13], vortex generators and

* Corresponding author. State Key Laboratory of Ocean Engineering and School of Naval Architecture, Ocean and Civil Engineering, Shanghai Jiao Tong University, Shanghai, 200240, China.

E-mail address: han.arkey@sjtu.edu.cn (Z. Han).

Nomenclature	
A	The amplitude of the surge motion [m]
C_p	Pressure coefficient [-]
c	Blade chord length [m]
D	Rotor diameter [m]
F_t	Total thrust of all blades [N]
k	Turbulent kinetic energy [m^2/s^2]
l_1	Winglet length 1 [m]
l_2	Winglet length 2 [m]
l_3	Winglet length 3 [m]
l_4	Winglet length 4 [m]
M_h	Bend length of winglet [cm]
P	Local static pressure [Pa]
P_∞	Free-stream static pressure [Pa]
P_w	Power [kW]
r	Spanwise height of the blade [m]
R	The radius of the rotor [m]
Re	Reynolds number [m]
sy_1	Section 1 along the spanwise direction of the winglet [m]
sy_2	Section 2 along the spanwise direction of the winglet [m]
sy_3	Section 3 along the spanwise direction of the winglet [m]
T_s	Period of surge motion [s]
t	Time [s]
U_∞	Wind speed [m/s]
u	Velocity component in the x -axis direction [m/s]
u^*	Friction velocity at the nearest wall [m/s]
V_s	The velocity of surge motion [m/s]
v	Velocity component in the y -axis direction [m/s]
w	Velocity component in the z -axis direction [m/s]
X_s	x -axis displacement of the motion of the turbine [m]
y^+	Dimensionless distance to the nearest wall [-]
Greek letters	
ρ	Fluid density [kg/m^3]
ζ	Performance parameter [-]
ω	Turbulent energy dissipation rate [-]
ω_h	Angular velocity of the rotor [r/s]
ν	Fluid viscosity [$\text{Pa}\cdot\text{s}$]
Δy_1	The grid scale of the boundary layer [m]
ΔP_w	Increment of power [-]
ΔF_t	Increment of thrust [-]
ΔP_{wi}	Increment of power coefficient 2 [-]
ΔF_{ti}	Increment of thrust coefficient 2 [-]
Abbreviations	
3-D	Three-dimensional
BEM	Blade element momentum theory
CFD	Computational fluid dynamics
C30T10	Winglet with cant = 30° and twist = 10°
DES	Detached Eddy Simulation
HAWT	Horizontal-axis wind turbine
MBH2	Bent winglet with $M_h = 2$ cm
NREL	National Renewable Energy Laboratory
SST	Shear stress transport
URANS	Unsteady Reynolds Averaged Navier Stokes
VC30I75	Double winglet with cant = 30° and cant2 = 75°
VAWT	Vertical-axis wind turbine

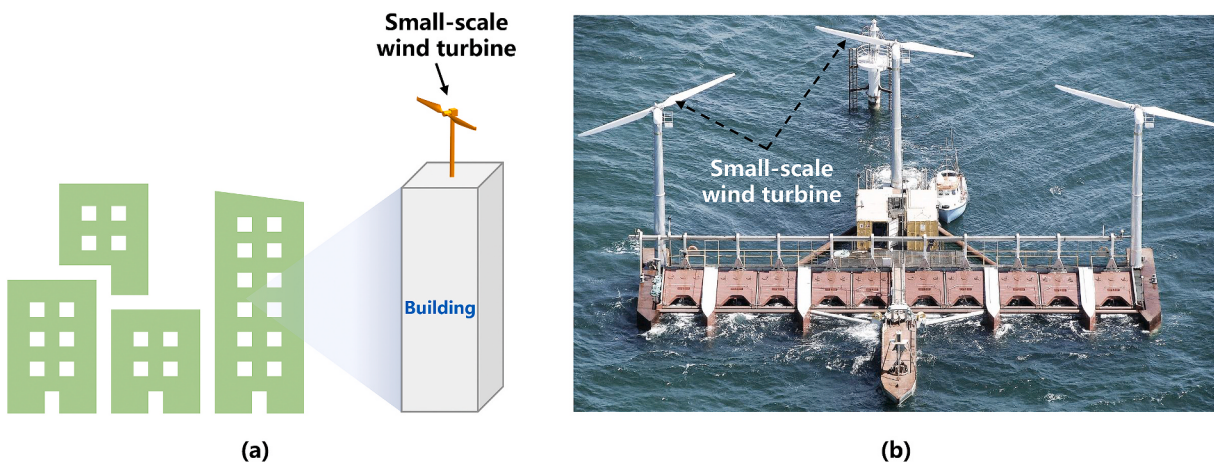


Fig. 1. Schematic diagram of the potential application scenarios of small HAWT (not to scale): (a) on the rooftops; (b) the combined wave and wind farm of Poseidon P-37 [8].

vortilons [14], ducted diffusers [15], and winglets [16], among others. These optimization measures have significant potential for future application to large wind turbines. The tip design of the blade has attracted wide attention among these strategies.

In the case of the tip of the blade, not only do the pressure differences at that location create the force, but usually the spanwise flow exists. This spanwise flow at the tip of the blade induced the tip vortices [17]. Vortices were considered to be the source of induced drag and reduced lift. Therefore, a proper blade tip design was able to reduce induced drag and improve aerodynamic performance [18]. Winglets had been used earlier in HAWTs. The design of the winglet was introduced into the

performance improvement of the airplane. According to Maughmer [19, 20], several keys that could be investigated for winglets are as follows: (1) translational parameters: planform configurations (different shapes), winglet height; (2) rotational parameters: cant angle, twist angle, toe angle, and sweep angle. These parameters played an important role in the performance of the winglets. To reduce the effect of induced drag, it could be controlled by the platform configuration, however, the planform configuration induced a surge of the drag that affected the winglet performance, as well as the winglet height. The load distribution on the winglet was managed by the sweep and twist angles, a reasonable arrangement could avoid stall flow. The toe angle was dependent on the

Table 1
Geometrical parameters of the Phase VI wind turbine [41].

Parameters	Values
Number of blades	2
Rotor diameter	10.058 m
Rpm	71.63 rpm
Cut-in wind speed	5 m/s
Rated power	19.8 kW
Cone angle	0°
Rotor location	Upwind
Power regulation	Stall regulated
Blade tip pitch angle	3°
Blade profile	S809

aerodynamic characteristics of the winglet, affecting its load distribution along the wing [21]. The direction of fluid flow on the wing surface was governed by the cant angle. Hence, the elimination of the aerodynamic problems of the HAWT and the improvement of its performance is of great importance.

To reach this desired outcome, three main methods were employed: model experimental method, theoretical model method, and computational fluid dynamics method (CFD) [15]. Wind tunnel experiments were difficult to observe the detailed flow behavior on the blade surface under complex conditions, requiring more advanced measurement techniques. Tip loss effects were common in wind turbine blades, which could lead to inaccuracies in the predictions of the blade element momentum (BEM). Although some modifications had been made to BEM, such as Prandtl's tip loss correction [22], this approach heavily relied on empirically tuned correction parameters [23]. It was reported by Ref. [24] that the measured shaft torque cannot be matched by the BEM when the wind speed exceeds 7 m/s, thanks to the dominant rotational effects. In addition to providing valuable insights into the aerodynamics and wake of wind turbines, the CFD method had the added advantage of displaying streamlines, pressure, and velocity contours that reflect actual flow conditions [25]. Unsteady Reynolds Averaged Navier-Stokes (URANS) and Large Eddy Simulation (LES) turbulence models were

widely used in CFD simulations [26]. URANS requires a lower grid resolution than LES, which reduces computational resources, and its time-averaged physical field is accurate. In addition, the LES or Detached Eddy Simulation (DES) model is widely used in scaled models, requiring significant computing resources. URANS SST $k-\omega$ model is a two-equation hybrid method and also an economical model, with reliable precision [27].

Based on the three main categories of research methods summarized above, to improve the power efficiency of wind turbines, the aerodynamic characteristics of wind turbines with winglets had also been investigated by a great number of scholarly individuals [28,29]. Based on the software Star CCM+, Miao et al. [30] investigated the comprehensive performance of wind turbine blades with 20 different tips. The configuration of streamlined endplates was found to can improve blade lift, and the winglet with thinner trailing edges showed significant performance improvements. Zhang et al. [31] used the orthogonal experimental design method with CFD as a platform to investigate the power gain performance of wind turbine blades with six different winglets. The twist angle of the winglets was found to be the most important factor among six sets of parameters. Improperly designed winglets could lead to a degradation of blade performance. By extending the blade tip to the pressure or suction side, induced drag caused by the blade tip vortex could be reduced, and additional lift would be generated, which enhanced the torque [32]. Zhu et al. [33] found that better lift improvements could be achieved by mounting winglets on the pressure and suction sides of the blade for HAWTs. The mechanism of winglets is to reduce the tip loss effect of the blade, improving the performance behavior of HAWTs [34,35]. Elfarra et al. [36] designed and optimized the aerodynamics of winglets for the blades of HAWTs and study their impact on power generation. The optimization was performed for three different wind speed conditions, resulting in a power gain of 9% with the implementation of the winglets. Farhan et al. [16] investigated the power enhancement effect of winglets with different winglet heights, cant angles, planform shapes, and airfoil shapes using the Phase VI case. The study revealed that the best

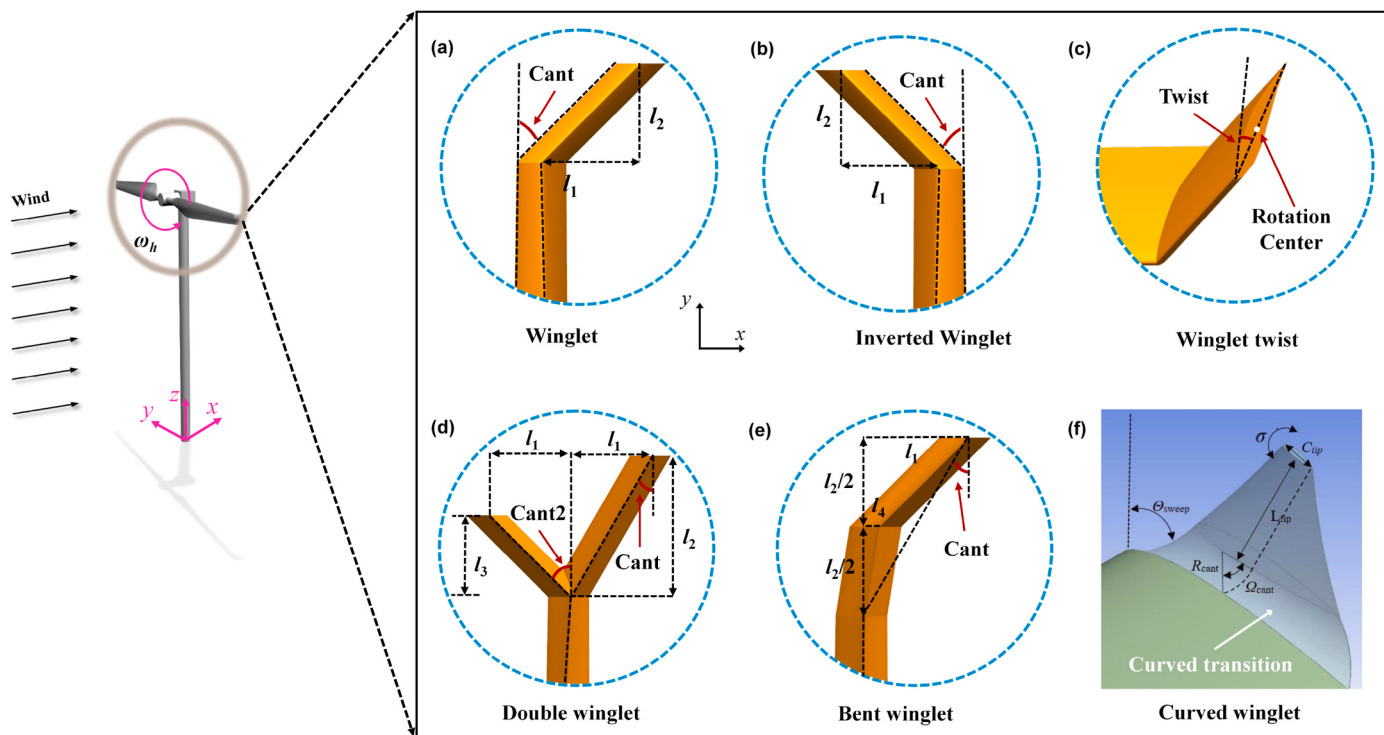


Fig. 2. Schematic diagram of wind turbine with winglet: (a) cant of traditional winglet; (b) cant of inverted winglet; (c) twist of traditional winglet; (d) cant of double winglet; (e) cant of bent winglet; (f) curved winglet accessed from [31].

Table 2

List of parameters of the winglet in different configurations: (1) cant angle: the negative sign indicates that the winglet extends in the opposite direction of the x -axis shown in Fig. 2(b); (2) twist angle: the negative sign is clockwise from the right-hand principle; l_2 can be obtained from l_1 as follows: $l_2 = l_1 / \tan(\text{Cant})$ in current study.

Cases	Cant angle/ $^{\circ}$	Winglet length (l_1)/cm	Twist/ $^{\circ}$	Wind speed/(m/s)	Number of winglets	
Configuration 1	30/-30	15/15	0/0	7/7	1/1	
	45/-45	15/15	0/0	7/7	1/1	
	60/-60	15/15	0/0	7/7	1/1	
	75/-60	15/15	0/0	7/7	1/1	
	30/-30	4.02/4.02	0/0	7/7	1/1	
	45/-45	8.66/8.66	0/0	7/7	1/1	
	60/-60	15/15	0/0	7/7	1/1	
Configuration 2	75/-60	25.98/25.98	0/0	7/7	1/1	
	30/45/60	15/15/15	-10/-10/-10	7/7/7	1/1/1	
	30/45/60	15/15/15	-6/-6/-6	7/7/7	1/1/1	
	30/45/60	15/15/15	3/3/3	7/7/7	1/1/1	
	30/45/60	15/15/15	6/6/6	7/7/7	1/1/1	
	30/45/60	15/15/15	10/10/10	7/7/7	1/1/1	
	30	15	10	5~15	1	
Configuration 3 (l_3/cm)	3.32/3.32	30	15/15	0/0	7/7	2/2
	(-75)/75					
	(-30)					
	5/5	30	15/15	0/0	7/7	2/2
	(-60)/60					
	(-30)					
	8.66/8.66	30	15/15	0/0	7/7	2/2
Configuration 4 (l_4/cm)	(-45)/45					
	(-30)					
	15/15	30	15/15	0/0	7/7	2/2
	(-30)/30					
	(-30)					
	2 (-2)	30/30	15/15	0/0	7/7	1/1
	5 (-5)	30/30	15/15	0/0	7/7	1/1
7.5 (-7.5)	30/30	15/15	0/0	7/7	1/1	
	10 (-10)	30/30	15/15	0/0	7/7	1/1
2	30	15	0	5~15	1	

performance was achieved when a 15 cm rectangular winglet with S809 airfoil and cant = 45° was employed.

Besides the above-mentioned traditional winglet design, some novel wing tip designs have been equally noticed. For example, O-tip and spiroid tip, the O-tip design was derived from some conceptual designs of aircraft [37] to improve aircraft performance; while the latter was proposed by Ref. [38] from a bionic spiral tip taken from a bird's wing tip to improve the lift performance of aircraft wings. The British

Experimental Rotor Program (BERP) [39,40] developed several helicopter blade tips based on three-swept wing tips to improve hover performance. These blade tip designs can also be used to optimize the design of wind turbine blades [30], with a power gain of 8.59%.

While previous studies have looked into the potential power boost of winglets, the focus has been exclusively on fixed wind turbines and conventional winglets. Consequently, there is a significant gap in our understanding of the power-boosting capabilities of floating wind turbines equipped with modified winglets. The constraints of the previous investigations should be addressed to fully explore the power-boosting potential of this new technology. Below, we outline the key factors that require attention to achieve a comprehensive understanding of the matter:

- The selection of a promising winglet is of paramount importance for the subsequent design. Nonetheless, a thorough comparison of various fundamental airfoils is yet to be carried out.
- Most of the existing studies on winglet optimization have focused on fixed wind turbines. However, it is also necessary to optimize winglets for floating wind turbines with platform motion characteristics.
- Numerous studies have been conducted on the parameter analysis of conventional airfoils, yet there is a dearth of research on the development of novel winglet designs.

In this study, a novel bent winglet blade will be proposed to enhance the performance of the traditional HAWT under platform motion. The NREL Phase VI wind turbine served as the baseline, and a comparison is made between the effects of conventional winglets, V-shaped double winglets, and the new bent winglets on the power gain effect of HAWTs. Furthermore, the study explores the effect of platform motion on the power gain effect of the optimal winglet. The power performance enhancement of the wind turbine is also focused on the cant angle and twist angle of the traditional winglet configuration. CFD software Star CCM+13.06 is used for modeling, calculation, and analysis of HAWTs with winglets. The URANS Shear Stress Transport (SST) $k-\omega$ model is employed in this study to close the Navier-Stokes equations and obtain detailed aerodynamic characteristics of the wind turbine.

The remaining sections of the current study are structured as follows: Section 2 presents the geometric models of the HAWT with different winglets and the numerical method, including the computational domain, mesh topology, and solver settings. Section 3 covers the mesh independence test and solution validation. Section 4 includes the comparison of different types of basic winglets, a comparison of optimization results of the bent winglet under different wind speeds, and a performance evaluation of the bent winglet under surge motion. Finally, Section 5 provides concluding remarks.

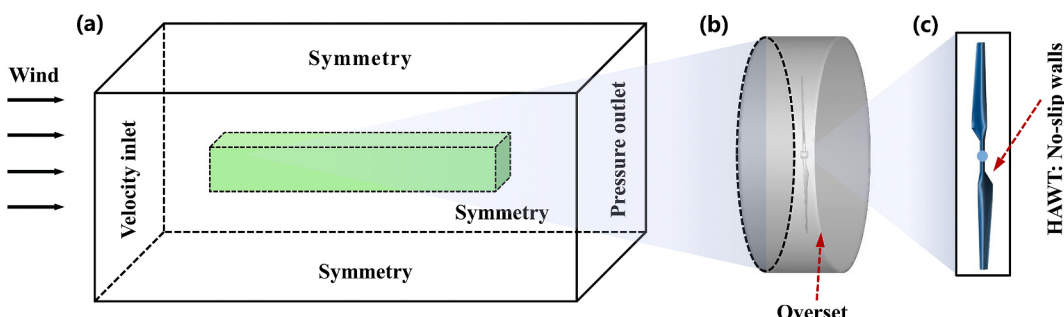


Fig. 3. Setting of computational domains: (a) overview; (b) rotational domain; (c) blade surface of Phase VI wind turbine.

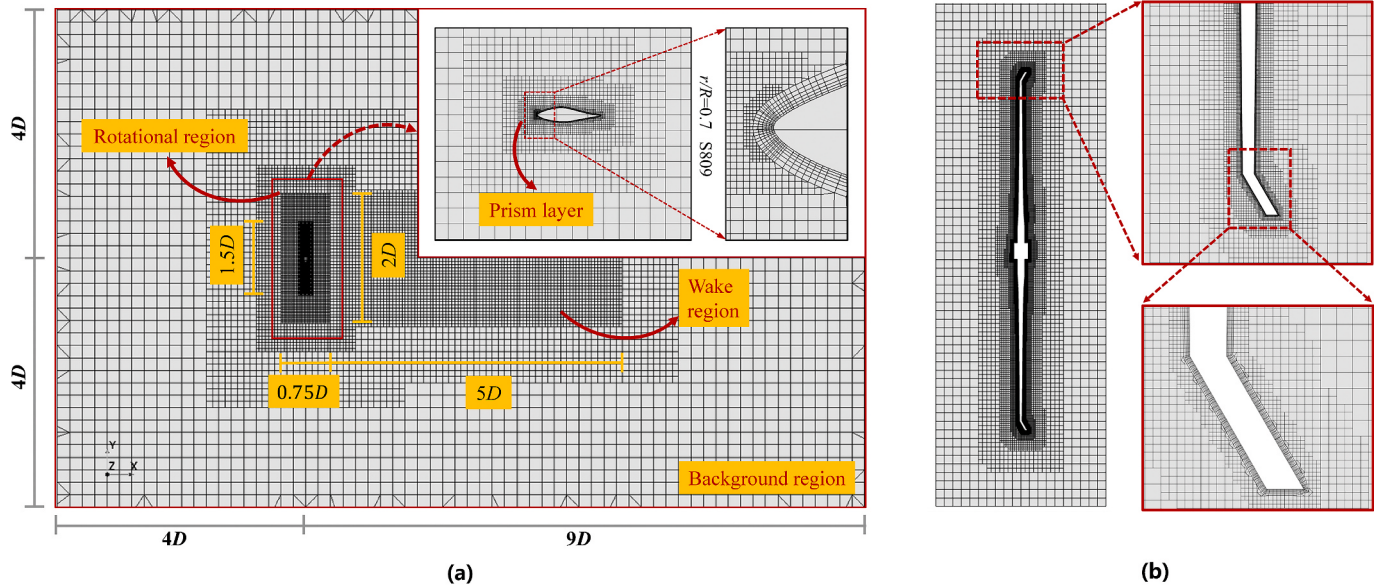


Fig. 4. Mesh topology at the plane of $y = 0$ both for baseline case and winglet case: (a) mesh of baseline; (b) mesh near the winglet.

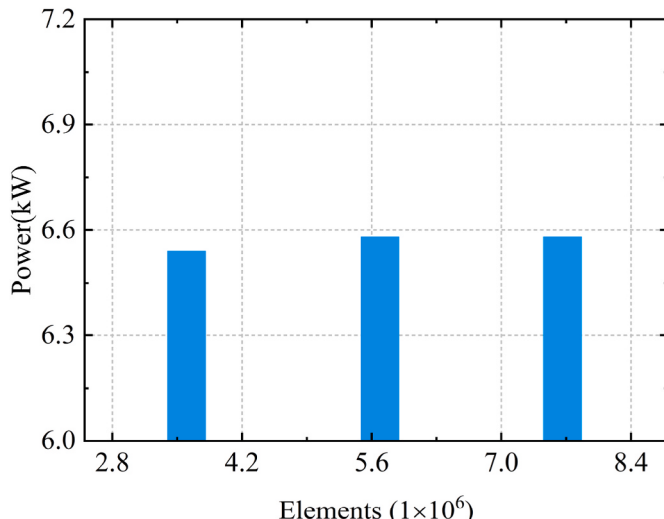


Fig. 5. Comparison of calculated power of Phase VI for different grid resolutions at a wind speed of 7 m/s.

2. Physical and numerical models

2.1. Blade with different winglet

The Phase VI wind turbine [41], designed by the National Renewable Energy Laboratory (NREL), is selected as the reference turbine. Due to its excellent performance and abundant experimental data, it has been utilized by many scholars for research [11,42]. The Phase VI wind turbine comprises two blades with a rotor diameter of $D = 10.058$ m and a rated power of 19.8 kW. Table 1 provides detailed parameters for Phase VI.

Three different configurations of winglets have been designed to improve the aerodynamic performance of Phase VI wind turbine blades, as depicted in Fig. 2. The winglets are installed at the tip of the blades, and their 3-D structures are obtained by extending them along their height direction. The S809 airfoil has been utilized for all of the winglets. The detailed settings for all cases in the current study are presented in Table 2.

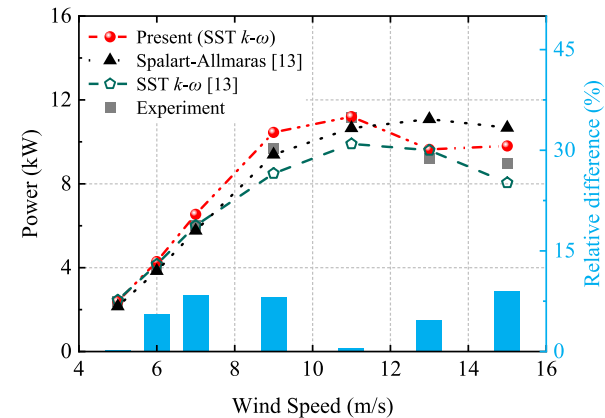


Fig. 6. Comparison of calculated and measured power using RANS turbulence models ($U_{\infty} = 7$ m/s): CFD findings come from Ref. [16]; the experimental data is acquired from Ref. [41].

2.1.1. Basic winglet

The design of blade tips for horizontal axis wind turbines (HAWTs) can be classified into three categories [30]:

- (i) Modifying the blade tip's geometric profile in the rotating plane, for example, by using swept, elliptical, or parabolic shapes.
- (ii) Projecting the blade tip beyond the rotating plane, as exemplified by winglets.
- (iii) Adding supplementary tip components, including endplates, Mie-type tip vanes, and so on.

The study conducted by Ref. [16] focuses on three parameters of winglet design: extension direction, cant, and twist, with a winglet length of 15 cm. In this configuration, the winglet extends towards the suction side of the blade (in the positive direction of the x -axis) and is referred to as the basic winglet (Fig. 2(a)) in the current study, while the opposite direction settings are referred to as inverted winglets (Fig. 2(b)). The study only considers variations in the parameters of cant (ranging from 30° to 75°) and twist (ranging from -10° to 10°), as displayed in Fig. 2(c). The magnitude of the cant angle is controlled by l_1 and l_2 using the control variable method. The study separately takes into

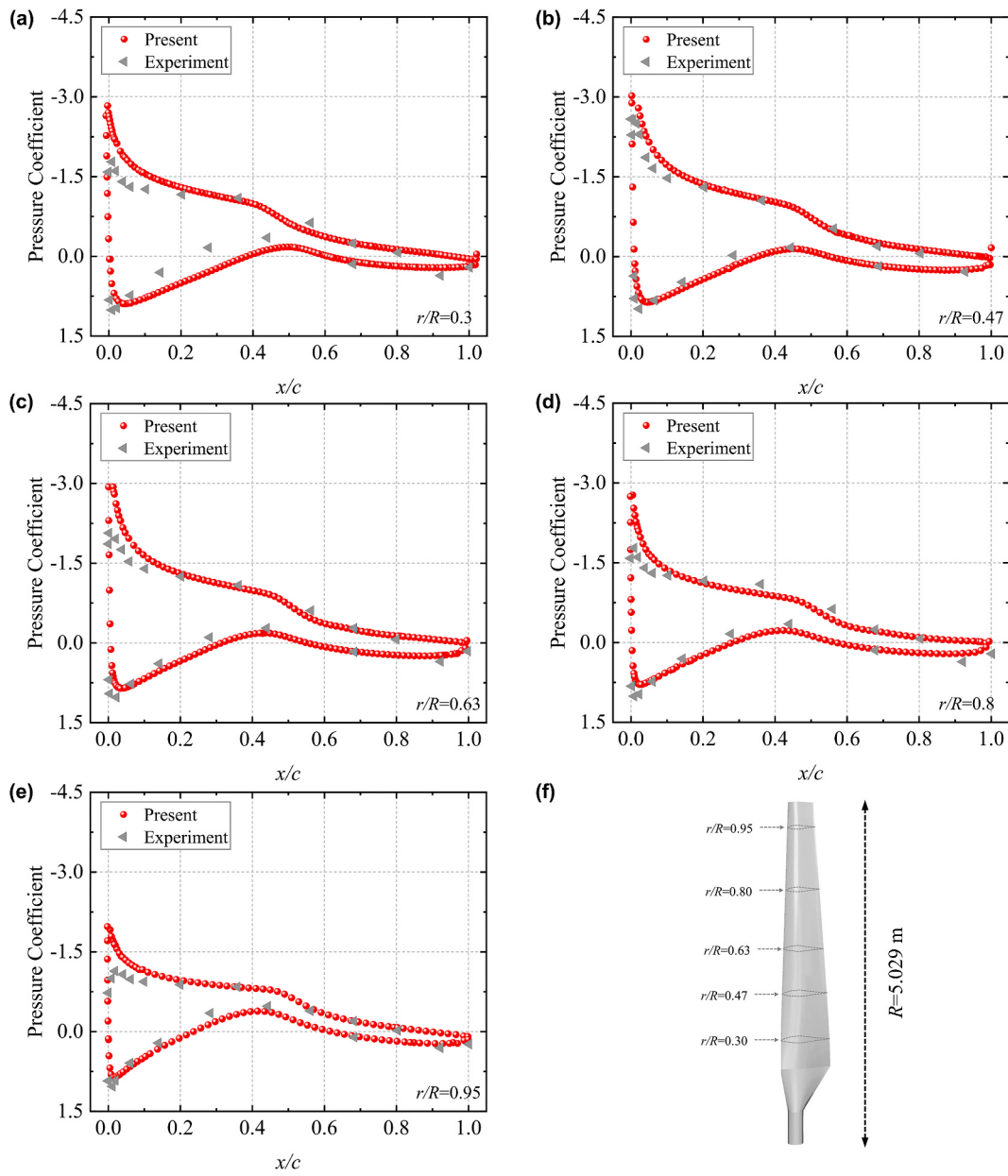


Fig. 7. Comparison of CFD and measured pressure coefficients of blade surface at $U_{\infty} = 7$ m/s: the experimental data is acquired from Ref. [41].

account the effect of modifying l_1 and l_2 alone on the power gain of HAWT.

2.1.2. V-shaped double winglet

The design of V-shaped double winglets is derived from the basic winglet, as shown in Fig. 2(d). In this study, the double winglet design features a fixed cant angle of 30° ($l_1 = 15$ cm) with only cant2 being modified by four different values of cant2 = 30° – 75° . V-shaped winglets have been previously investigated and applied in vertical axis wind turbines by researchers, including Ref. [43].

2.1.3. Bent winglets

In this subsection, a new type of winglet, the bent winglet, is proposed based on the previous basic winglet design. The bent winglets are bent at the midpoint of their height, as shown in detail in Fig. 2(e), and seven different lengths of l_4 (ranging from –10 cm to 10 cm) are designed. When the bending length l_4 at the middle of the winglet is negative, it extends to the pressure side of the blade. Determine the

optimal set of bending lengths that maximizes the power gain of the winglet as the objective. As opposed to the curved winglet proposed by Ref. [31]; the current bent winglet is polyline shaped and is easy to design and manufacture, as depicted in Fig. 2(e).

2.2. Numerical solutions

Commercial computational fluid dynamics (CFD) software Star CCM+ is adopted and coupled with overlapping grid technology. The fluid is considered incompressible and the Navier-Stokes equation is combined with Reynolds decomposition treatment in this study. Moreover, the unsteady Reynolds-Averaged Navier-Stokes (URANS) equations are implemented using Star-CCM+ 13.06. The $k-\omega$ shear stress transport (SST) model, which is widely used to solve the rotating blade problems in wind turbines due to its high reliability [26,44], is employed to close the URANS equations. Furthermore, the Spalart-Allmaras model, which solves a single transport equation to calculate the kinematic vortex viscosity, is also economical. The SST $k-\omega$

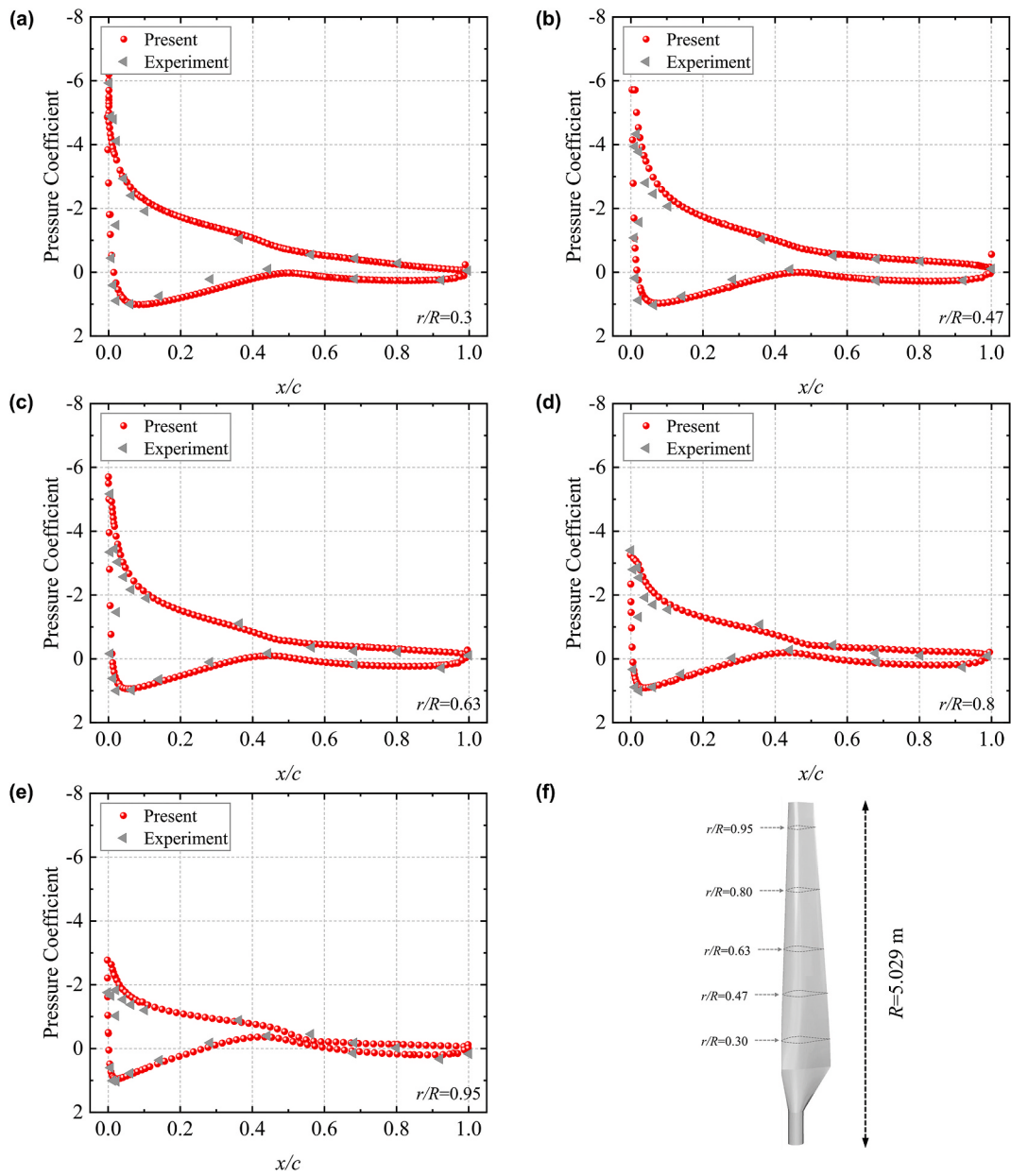


Fig. 8. Comparison of CFD and measured pressure coefficients of blade surface at $U_{\infty} = 9$ m/s: the experimental data is acquired from Ref. [41].

model is a two-equation hybrid method, with higher precision [16]. The comparison results of different models can be discussed in Section 3.2.

2.3. Computational domain

The computational domain used in the study is shown in Fig. 3. The inlet of the domain is defined as a velocity inlet with values of $u = U_{\infty}$, $v = 0$, and $w = 0$, while the outlet is set as a pressure outlet with a pressure of 0. The other boundaries are defined as symmetry conditions, aiming to avoid the wall reflection effect [15,45]. The surface of the wind turbine is considered a no-slip wall with values of $u = 0$, $v = 0$, and $w = 0$. The origin of the Cartesian coordinate system is located at the center point of the wind turbine hub. The distance from the upstream and lateral boundaries is $4D$, and the length from the origin to the outlet is $9D$. The wake region of the HAWT is accurately captured by encrypting the grid of the wake region, with a size of $\Omega_1[5D, 2D, 2D]$. In the current study, the inflow turbulence intensity is 1% in all cases.

The radius of the cylindrical rotation domain is D , and the thickness

is $0.75D$, while the turbine motion is realized using the overset mesh technique. Overlapping meshes allow for flexible handling of motion problems, with independent meshes in each sub-region allowing for unconstrained relative displacement [46]. The overlapping meshing technique is widely used in the simulation of complex moving bodies. However, it also requires higher differential accuracy and consumes larger computational resources. A structured grid is employed to discretize the three regions, as illustrated in Fig. 4. The grid near the wall generates y^+ values greater than 30, combined with six prismatic layers adjacent to the blade surface. The total boundary layer thickness is 0.0125 m ($1.24 \times 10^{-3}D$) for the blade surface at $r/R = 0.7$ ($Re = 9.24 \times 10^5$), and the growth rate is 1.2, resulting in a total number grid of 5.7×10^6 . The high $y^+ = (u^* \Delta y_1)/v$ wall treatment is suitable for cases where turbulence is not well damped in the near-wall region [26], where u^* and Δy_1 denote the friction velocity at the nearest wall, and the grid scale of the boundary layer, respectively. Although this treatment may provide a relatively inaccurate result on the drag force of blades in the current simulation, the velocity near the blade tip region is very high,

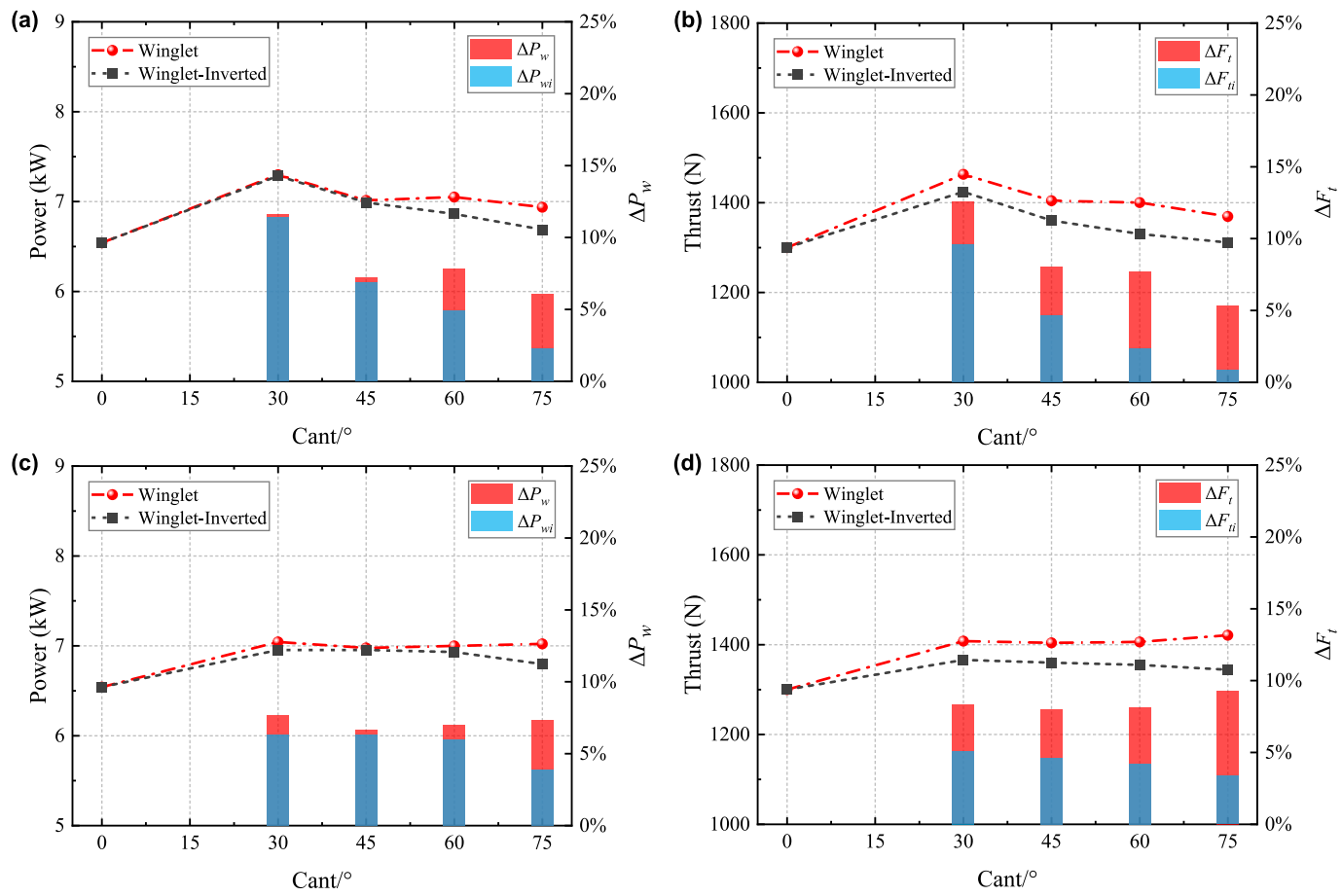


Fig. 9. The effect of cant on power and thrust of HAWT with winglet: (a) and (b) cases of fixed l_1 ; (c) and (d) cases of fixed l_2 .

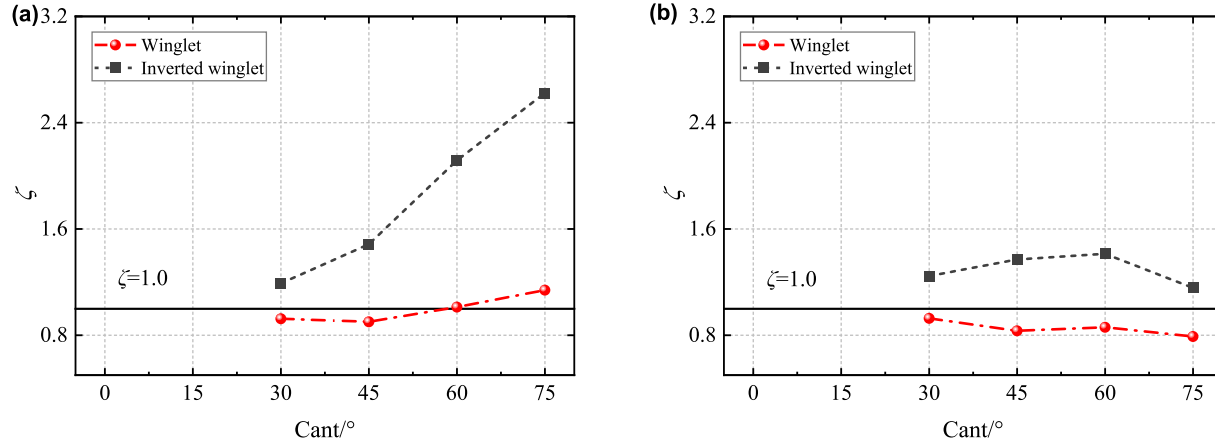


Fig. 10. The effect of cant on ζ for HAWT with winglet: (a) cases of fixed l_1 ; (b) cases of fixed l_2 .

rendering this drag force negligible when compared with the lift force in such a high Reynolds number. A wall function for a high Reynolds number is initiated in the logarithmic region of the boundary layer, requiring the wall y^+ of the ground surface to be greater than 30.

Previous studies have utilized rotor rotation time steps of 3° or 4° [47,48]. However, in this study, a time step of every 1° rotation of the HAWT is employed, corresponding to approximately 2.32677×10^{-3} s, with each time step being calculated using 20 iterations. This ensures a more accurate simulation of the HAWT, whose full rotation period is 0.8376 s. All the simulations are done on a server with two Intel(R) Xeon(R) CPUs (E5-2673 v3, 2.40 GHz), the physical time required to

calculate one revolution is about 6 h. The time step size of 2.32677×10^{-3} s is fixed for all simulations in this study. A detailed sensitivity test of the time step is provided in Appendix A.

3. Simulation verification and validation

3.1. Grid convergence study

A straight-forward approach to determining the discretization error in CFD simulations is through convergence examination. As the grid is refined, the temporal discretization errors should asymptotically

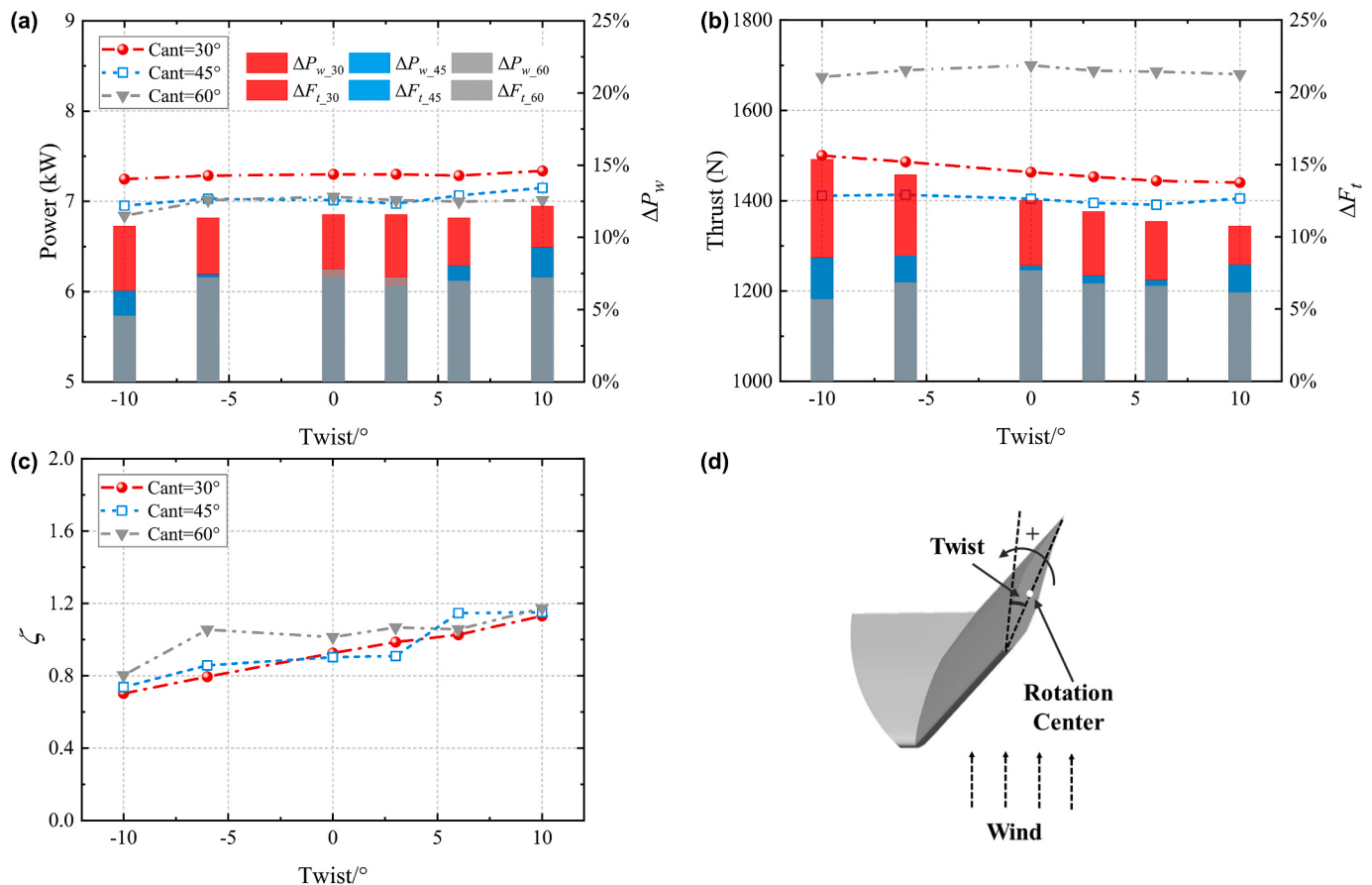


Fig. 11. The effect of twist on power and thrust of HAWT with winglet: (a) power; (b) thrust; (c) ζ ; (d) schematic diagram of twist.

approach zero, respectively, except for the computer round-off error. Fig. 5 demonstrates the comparison of the power ($P_w = Q \cdot \omega_h$, where Q is torque of wind turbine and ω_h denotes rotational speed) with different grid resolutions (Fine mesh, medium mesh, and coarse mesh). In different configurations of the grid, the settings of the blade boundary layer are maintained unchanged, and the remaining grid dimensions are used as variation parameters. The results for the medium and fine meshes are quite similar, while the coarse mesh results in an underestimation of the torque. As a result, considering mesh independence and computational efficiency, the medium mesh is utilized for all subsequent simulations in this study.

3.2. Validation using experimental data

Fig. 6 demonstrates the comparison of the baseline-based calculation results with experimental data [41] and other CFD results [16]. The current calculation overestimates the experimental and other CFD results, which could be attributed to ignoring the effect of the nacelle and the tower. However, the maximum value of the relative error is within 9% at the stall case ($U_\infty = 15$ m/s), which might be due to the inability of the large y^+ processing to accurately characterize the dynamic stall characteristics of the blade surface. The SST $k-\omega$ model exhibits superior performance in capturing the flow parameters in the pre-stall and stall regimes as compared to the Spalart-Allmaras model. Overall, the numerical model (SST $k-\omega$) applied in this study has considerable reliability. The calculated results are more approximate to the experimental data and are adopted in the cases used in this study.

Figs. 7 and 8 show a comparison of the calculated and measured blade surface pressure coefficients for wind speeds of 7 and 9 m/s. The pressure coefficient is calculated as follows:

$$C_p = \frac{P - P_\infty}{0.5\rho(U_\infty^2 + (\omega_h r)^2)} \quad (1)$$

where P is the local static pressure and U_∞ represents wind speed, separately; the free-stream static pressure is described as $P_\infty = 0$, ω_h is angular velocity and r is the axial distance from the center of the rotor at a certain section of the blade.

The results obtained from the URANS model in this study are generally in agreement with the wind tunnel test measurements. However, the pressure coefficients on the airfoil leading edge are slightly overestimated at different spanwise sections of the blade ($r/R = 0.3, r/R = 0.47, r/R = 0.6, r/R = 0.8, r/R = 0.95$) for the cases of $U_\infty = 7$ m/s and $U_\infty = 9$ m/s. This overestimation is also observed in other studies [11, 16]. In addition, the torque and thrust validation of the floating wind turbine under surge motion can be accessed in Appendix B.

4. Results and discussion

Before delving into the main discussion, it is necessary to establish a clear understanding of the relevant symbols. The power and the thrust of the rotor are denoted as P_w and F_t , respectively. ΔP_w indicates power increment based on baseline where the winglets extending in the suction side direction (Fig. 2(a)), ΔP_{wi} indicate the winglets extending in the pressure side (Fig. 2(b)). The meanings of the abbreviation ΔF_t and ΔF_{ti} are as before. Note that the discussion of the results in Sections 4.1~4.3 is based on the standard wind speed of 7 m/s.

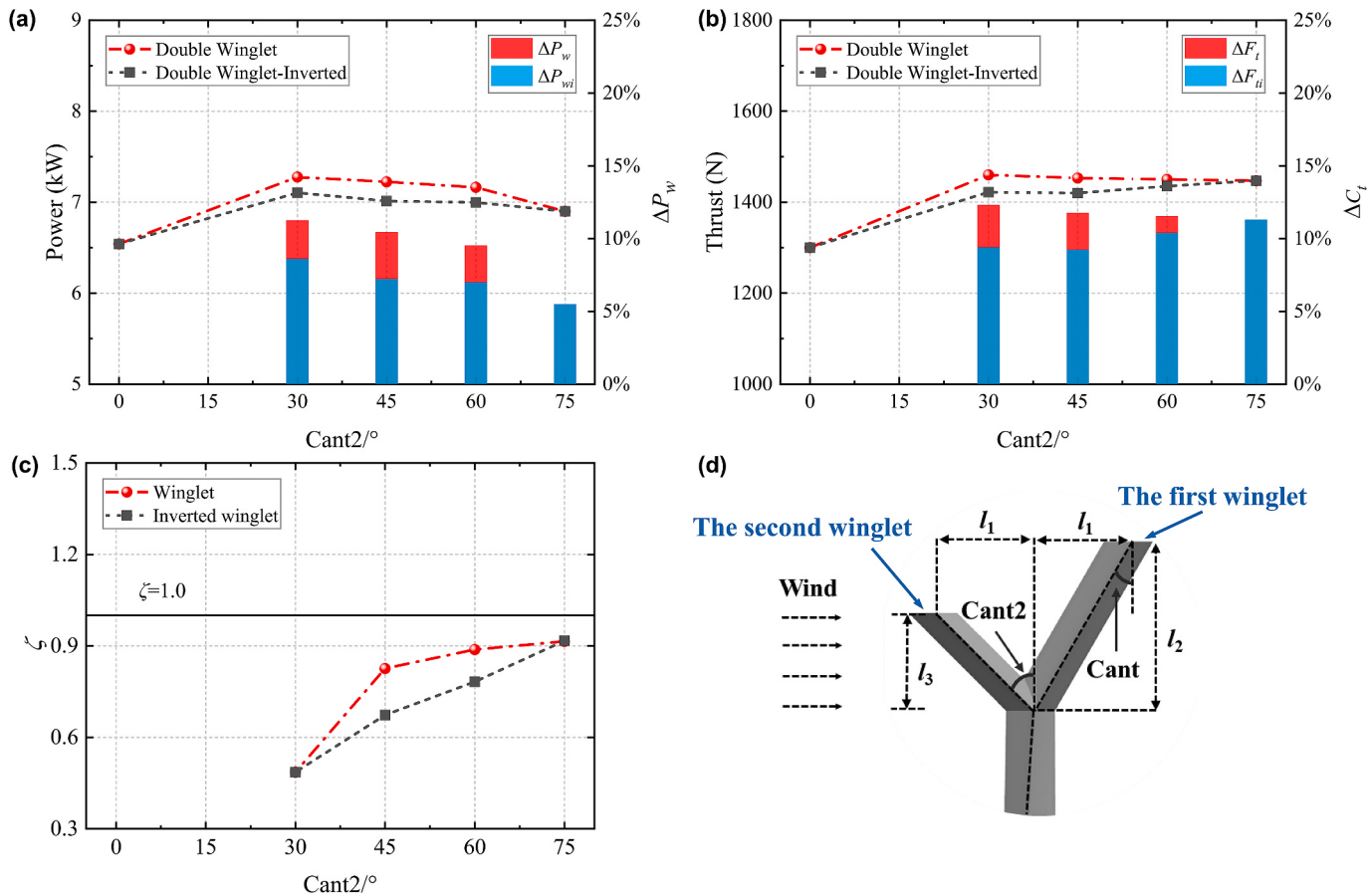


Fig. 12. The effect of double winglet on power and thrust of HAWT: (a) power; (b) thrust; (c) ζ ; (d) schematic diagram of the double winglet.

4.1. Performance improvement

4.1.1. Effect of cant

Fig. 9 presents the effect of winglets with varying cant angles on the power (P_w) and thrust (F_t) of the wind turbine. The configuration of the winglets includes the fixing direction (l_1 or l_2) and the mounting direction (suction side or pressure side). The results indicate that the P_w gain is greater in the case of fixing l_1 than in the fixed l_2 case, and the installation direction of the winglet also affects the P_w gain. The power gain is maximized when the winglets extend toward the pressure side of the HAWT blade, which also results in higher thrust.

As the cant angle increases while l_1 is fixed for cases with winglets extending to different sides, both P_w and F_t (shown in Fig. 9(a) and (b)) decrease. This is because the higher cant angle leads to a reduction in the swept area of the rotor, making it less power. The length of the winglet is thus a crucial parameter for improving the performance of the HAWT, as noted in previous literature [16]. However, it has been argued that winglets function as diffusion devices that move the vortex at the blade tip, reducing the tip loss and thus improving the HAWT's performance [34].

Fig. 9(c) and (d) illustrate that when l_2 is fixed, P_w and F_t exhibit only minor fluctuations within the cant angle range of 30°–75°. The adjustment of the cant angle does not impact the length of the winglet; therefore, it has limited influence on the rotor performance. However, the winglet installation results in a noteworthy increase in power gain compared to the baseline case, suggesting that the winglet installation can effectively reduce the blade tip loss.

Introducing the parameter $\zeta = \Delta P_w / \Delta F_t$ enables further evaluation of the winglet's performance. Results from Fig. 10 indicate that the ζ of winglets extending towards the pressure side is significantly larger than those extending towards the suction side. For fixed- l_1 cases, there is an

approximate positive relationship between ζ and the cant angle. While the winglet extending towards the pressure side exhibits a good comprehensive evaluation index ζ , its power gain effect is not as great as that of the winglet extending towards the suction side. When l_1 is fixed, the change in cant angle leads to an enlargement of the swept area of the rotor and causes a significant variation in torque and thrust; instead, when the winglet extends to the pressure side, the thrust of the rotor decreases with increasing cant, leading to an increase in ζ (Fig. 10(a)). When l_1 is fixed, the modification of the swept area of the rotor is smaller and has less effect on the torque and thrust of the rotor, so the alteration of ζ is less than the former (Fig. 10(b)).

In summary, the winglets are believed to enhance the P_w of HAWT through the combined effects of reducing blade tip loss and increasing swept area. The optimized power performance is demonstrated at cant = 30°, where the P_w of the cases with winglets extending to the suction side and pressure side increased by 11.6% and 11.3%, respectively, compared to the baseline case.

4.1.2. Effect of twist

In this subsection, three different cant angles (30°, 45°, 60°) are selected and equipped with six different sets of twist (-10°, -6°, 0°, 3°, 6°, 10°) respectively. $\Delta P_{w,30}$, $\Delta P_{w,45}$, $\Delta P_{w,60}$ represent the power gains of the wind turbine with winglets at 30°, 45°, and 60° cant angles, respectively. The best performance improvement is achieved (Fig. 11) when the twist angle at the blade tip of the winglet is positive, resulting in an increase of P_w by 12.1% at cant = 30° and twist = 10°. It is observed that the thrust shows a linear decreasing trend with the variation of twist for the case of cant = 30° and 45°, as shown in Fig. 11(b). However, for the case of cant = 60°, the implementation of the twist angle is detrimental to the power performance of the winglets, and its P_w reaches its maximum when it is twist-free (twist = 0°). The enlargement of twist

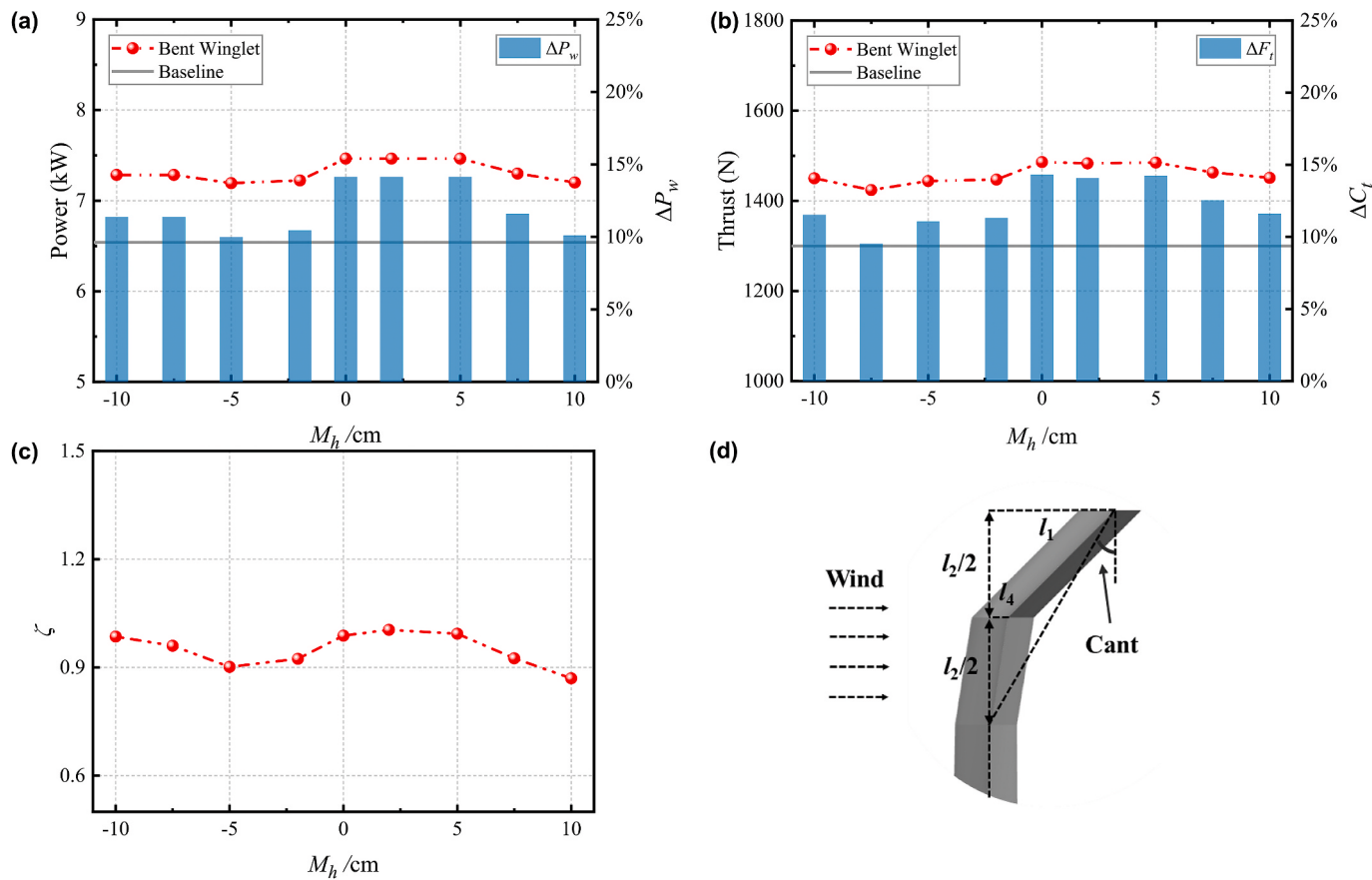


Fig. 13. The effect of bent winglet on power and thrust of HAWT: (a) power; (b) thrust; (c) ζ ; (d) schematic diagram of the bent winglet.

significantly contributes to the improvement of the load distribution on the winglet surface, with a more significant effect observed at cant = 30°.

The improvement of the composite index ζ clearly benefits from the expansion of the cant angle. The largest value of ζ , compared with other cases, is found to fluctuate with a twist at cant = 60°. In the case of cant = 30°, the comprehensive performance evaluation index ζ reaches 1.1 (Fig. 11(c)) when the twist is increased to 10°. Thus, the load on the wind turbine can be significantly reduced by increasing the twist angle of the winglet, while reducing the cant angle can enhance the energy capture performance of the wind turbine. The results obtained from this winglet configuration can provide a beneficial reference for the optimization of blade configuration in wind turbines.

4.1.3. Effect of double winglets

In this subsection, two double winglet mounting orientations are considered: (1) the first winglet extends towards the suction side and the second winglet extends towards the pressure side (Fig. 12(d)); (2) the first winglet extends towards the pressure side and the second winglet extends towards the suction side (Double winglet-inverted). In addition, only the cant of the second winglet is modified, while the cant of the first winglet is constantly equal to 30°.

For V-double-winglets indicated in Fig. 12, the power of the wind turbine increases similarly as cant2 increases, while the corresponding thrust remains almost independent of cant2. The optimal case (cant2 = 75°) results in a ΔP_w of 11.2%, based on the baseline case. However, this corresponds to a comparable level within ΔP_w compared to the results obtained with single winglets, as demonstrated in Subsections 4.1.1 and 4.1.2. ζ depicted in Fig. 12(c) shows an increasing trend as the Cant2 angle increases, but its magnitude is less than 1. Additionally, compared to conventional winglets, the V-winglets are more complex to install and

provide no significant improvement in aerodynamic performance.

4.1.4. Effect of the bent winglet

In this subsection, the baseline winglet is subjected to a bending process at the midpoint of its length for the cant = 30° case to create a bent winglet. The impact of bending parameter l_4 (M_h) on wind turbine performance enhancement is evaluated. The bending of the winglets leads to improvements in wind turbine performance as well as blade loading (as depicted in Fig. 13).

As M_h increases towards the pressure side ($M_h < 0$), the power gain performance of the winglet is significantly lower than that of $M_h > 0$. However, the case of $M_h = 10$ cm represents the worst power gain performance, even lower than the result of $M_h = -10$ cm. Additionally, the comprehensive evaluation coefficient ζ is at a minimum of 0.87 for $M_h = 10$ cm, while its maximum is 0.99 for $M_h = 2$ cm.

When M_h is in the range of 0 cm–5 cm, the P_w reaches its maximum value ($P_w = 7.46$ kW) with a ΔP_w of 14.1% compared to the baseline without winglet. By combining the optimization results from the previous winglets, the optimal case in this study is determined to be the bent winglet with $M_h = 2$ cm.

4.2. Pressure distribution of the winglets

To further investigate the aerodynamic characteristics of different winglet configurations, the traditional winglet with cant = 30° and twist = 10° is referred to as C30T10, the double winglet with cant = 30° and cant2 = 75° is abbreviated as VC30I75, and the bent winglet with $M_h = 2$ cm is denoted as MHB2. The winglet is evenly divided into four equal parts along its length using three cutting lines (sy_1 , sy_2 , sy_3).

In Fig. 14, the pressure coefficients of different sections (sy_1 , sy_2 , sy_3) along the spanwise direction of the winglet are extracted for the three

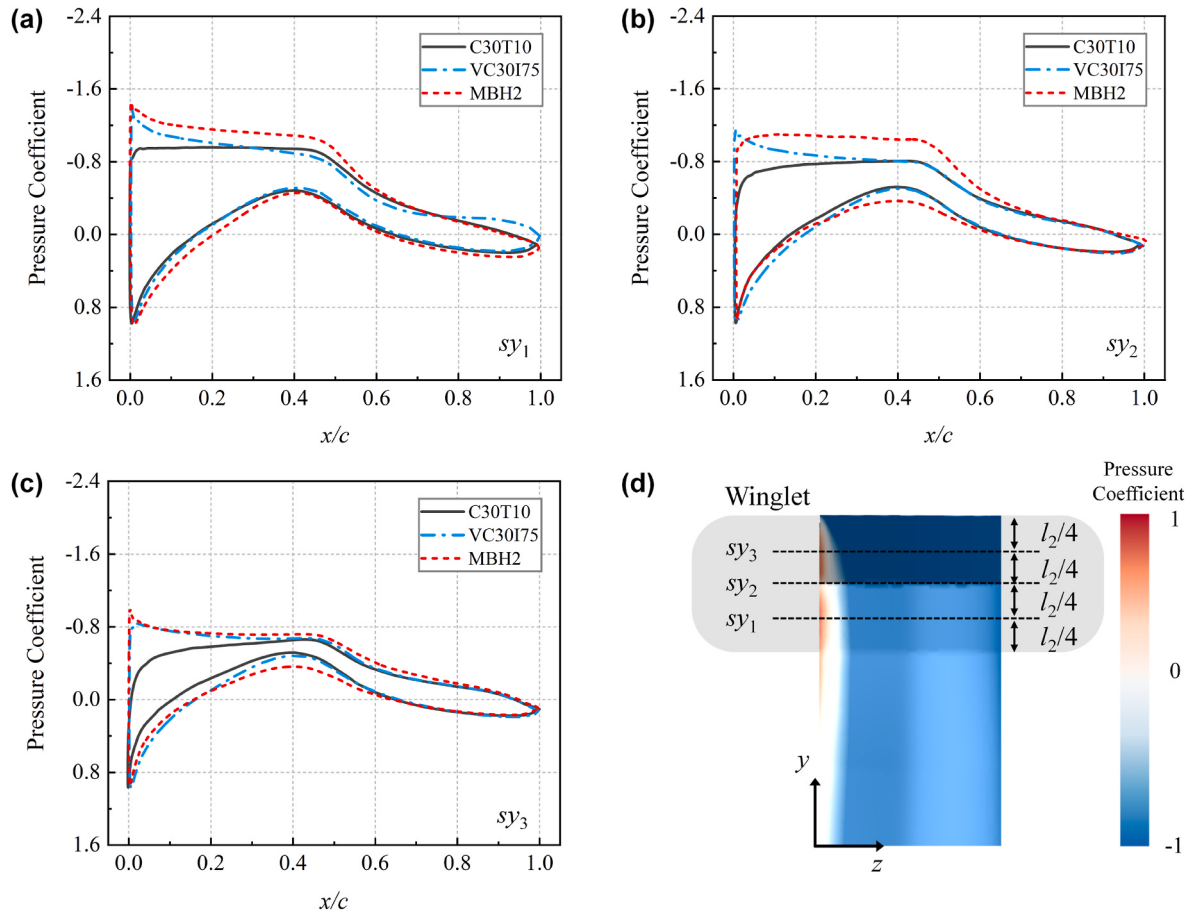


Fig. 14. Comparison of pressure coefficients of different winglets at different spanwise heights: (a) sy_1 (b) sy_2 ; (c) sy_3 ; (d) spanwise-section schematic.

optimal winglets to investigate their aerodynamic characteristics. The C30T10 winglet has the smallest pressure coefficient on the suction side among the three configurations, while the maximum pressure coefficient occurs in the case of MBH2. According to Ref. [16], a winglet platform can extract more energy from the fluid than a baseline winglet. The enhancement of the pressure coefficient indicates that the energy capture effect of different winglet configurations depends on the surface flow characteristics of the winglet. It can be inferred that the pressure coefficient on the suction side surface of the winglet has a positive effect on performance improvement.

Fig. 15 shows a comparison of the cross-sectional static pressure distribution at three different span sections for a more detailed analysis of the pressure distribution characteristics around the winglets. There are significant differences in the pressure distribution around the three winglets due to the geometry effect of the winglets. It is observed that the pressure distribution area near the leading and trailing edges of the wing is the largest for MBH2 at the same height position. The suction area on the suction side of the airfoil is also the largest for MBH2 among the three winglets.

4.3. Blade tip streamline

To investigate the power gain mechanism of winglets in different configurations, Fig. 16 presents three-dimensional streamline and vorticity distribution near the blade winglets. The flow field near the winglet illustrates the pressure distribution and aerodynamic performance characteristics. Differences in the flow field near the winglets are observed for the three different configurations, with the MBH2 showing the highest fluid energy absorption.

All configurations have vortices located near the blade tip due to the

wake-vortex structure consisting of blade tip vortices and hub vortices. In the C30T10 case, vortices are present on both sides of the winglet tip, while baseline tip vortices form only on the suction side of the winglet. In the VC30I75 case, the vortices are distributed on the suction side of the two winglet tips. The vorticity distribution characteristics of MBH2 are close to those of the baseline. Fig. 16 also plots a comparison of the iso-surface contours between the different configurations and the baseline when the Q-criterion value is 0.005. The position of the vortex structure formation for the case with a winglet is shifted downstream, indicating that the low-pressure region near the tip of the blade is formed further away.

4.4. Optimization for different wind speeds

The winglet optimization treatments previously discussed are all conducted at a wind speed of 7 m/s. This subsection presents a comparison of the power gain performance of two optimal winglet conditions (C30T10 and MBH2) at different wind speeds (5–15 m/s), including a comparison of the corresponding thrust, as illustrated in Fig. 17.

At various wind speeds, the wind turbine equipped with winglets demonstrates positive energy gain, with the MBH2 case exhibiting slightly better power gain than the C30T10 case. The highest power gain is achieved at a wind speed of 7 m/s for both winglet configurations, while the lowest power gain is observed at $U_\infty = 13$ m/s. Additionally, the presence of winglets increases the thrust of the wind turbine, causing the structure to endure a larger load compared to the baseline.

Compared to the optimal winglet configurations studied by Refs. [16, 36]; the corresponding ΔP_w of the optimal case in this study reaches 14.1%, owing to the enhanced pressure coefficient [16]. utilized a

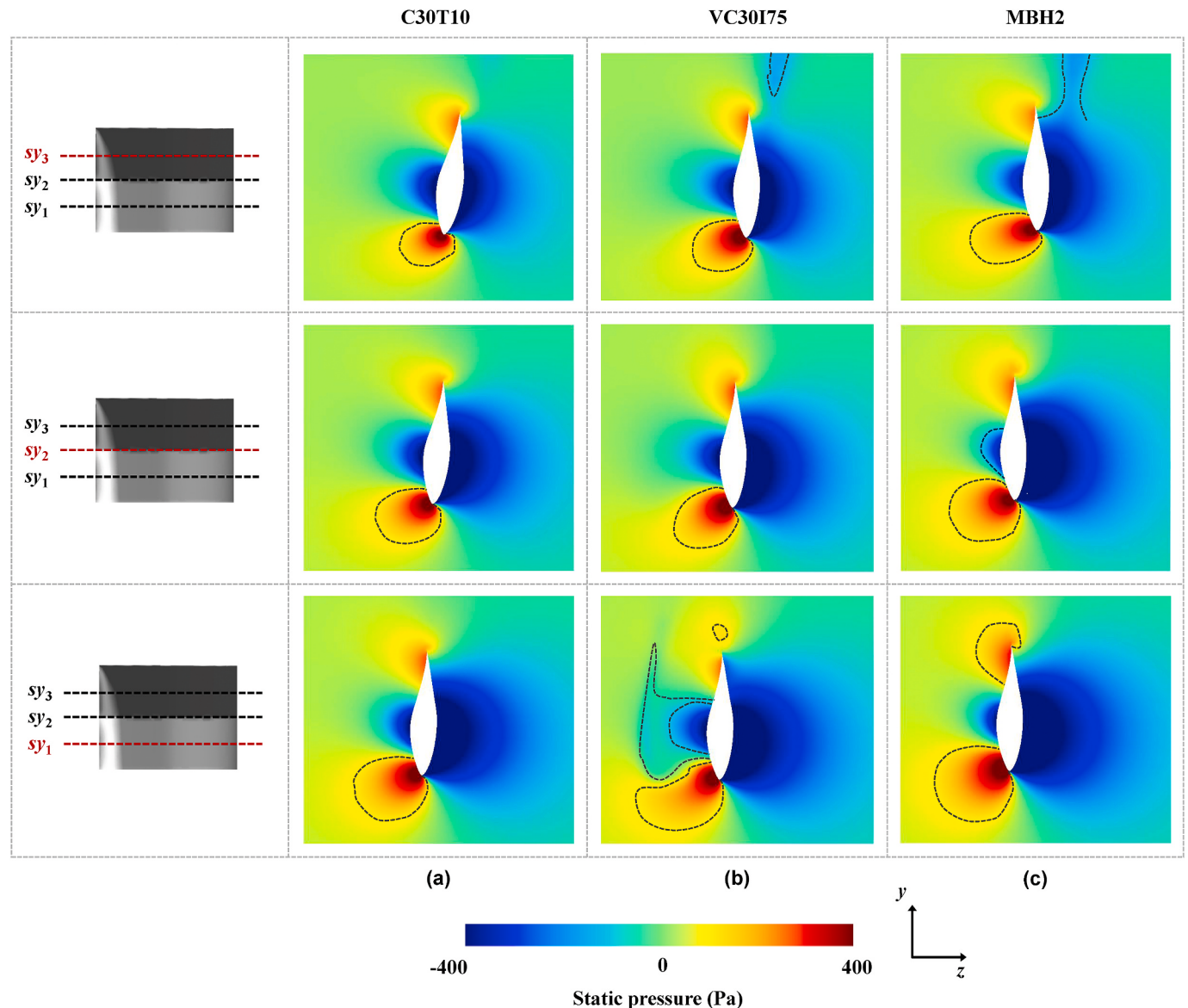


Fig. 15. Comparison of the sectional static pressure distribution of three different configurations at three different spanwise sections of blade: (a) C30T10; (b) VC30I75; (c) MBH2.

rectangular winglet with S809, with a cant angle extended toward suction of 45° and an extension length of 15 cm. In contrast, the winglet designed by Ref. [36] was generated by extending 7.5 cm to the suction side, with a cant angle and twist of 84° and 2° , respectively.

4.5. Winglet performance under surge motion

The platform motion affects the aerodynamic characteristics and wake characteristics of the offshore wind turbine. The examination of the power gain effect of winglets in fixed conditions is crucial, but it is also essential to investigate the power gain of wind turbine winglets with platform motion. Fig. 18 presents a comparison of the power and thrust between the optimal winglet design condition (MBH2) and the baseline under the surge motion. The platform motion is exclusively considered for the surge motion, with the motion amplitude $A = 0.03D$ [49] and motion period 2.988 s. The surge motion is implemented by a given pre-defined function (Appendix B). Notably, the platform motion can amplify the instantaneous power and thrust [50]. The instantaneous torque with the winglet is also larger than the standard case. The time-averaged power of the wind turbine with the winglet is 14.55%

higher than that of the baseline under the surge motion. The instantaneous torque and thrust with the winglet are also larger than the standard case. A 14.4% increase in time-averaged thrust is observed in the condition with winglets compared to the baseline.

The aerodynamic performance (torque and thrust) under different surge periods are analyzed in Fig. 19. With the reduction of the surge periods (increase in frequency), the fluctuation of the aerodynamic performance is also more intense, showing a strong interaction between the wind turbine blades and the incoming flow caused by the surge. The torque and thrust of the wind turbine are both positive, which does not belong to the vortex ring state mode, under various surge motion conditions.

Table 3 compares the power and thrust of MBH2 at different surge frequencies. When the period of the surge motion is reduced by 0.5 times, the average torque and thrust of the wind turbine are reduced by about 3% and 4%, respectively. However, the fluctuation of torque and thrust increased by 81% and 87.5%, respectively. The average change of aerodynamic force is small, but the fluctuation of aerodynamic force is reduced to at least half of the original period by increasing the period of surge motion to double the original period. In conclusion, increasing the

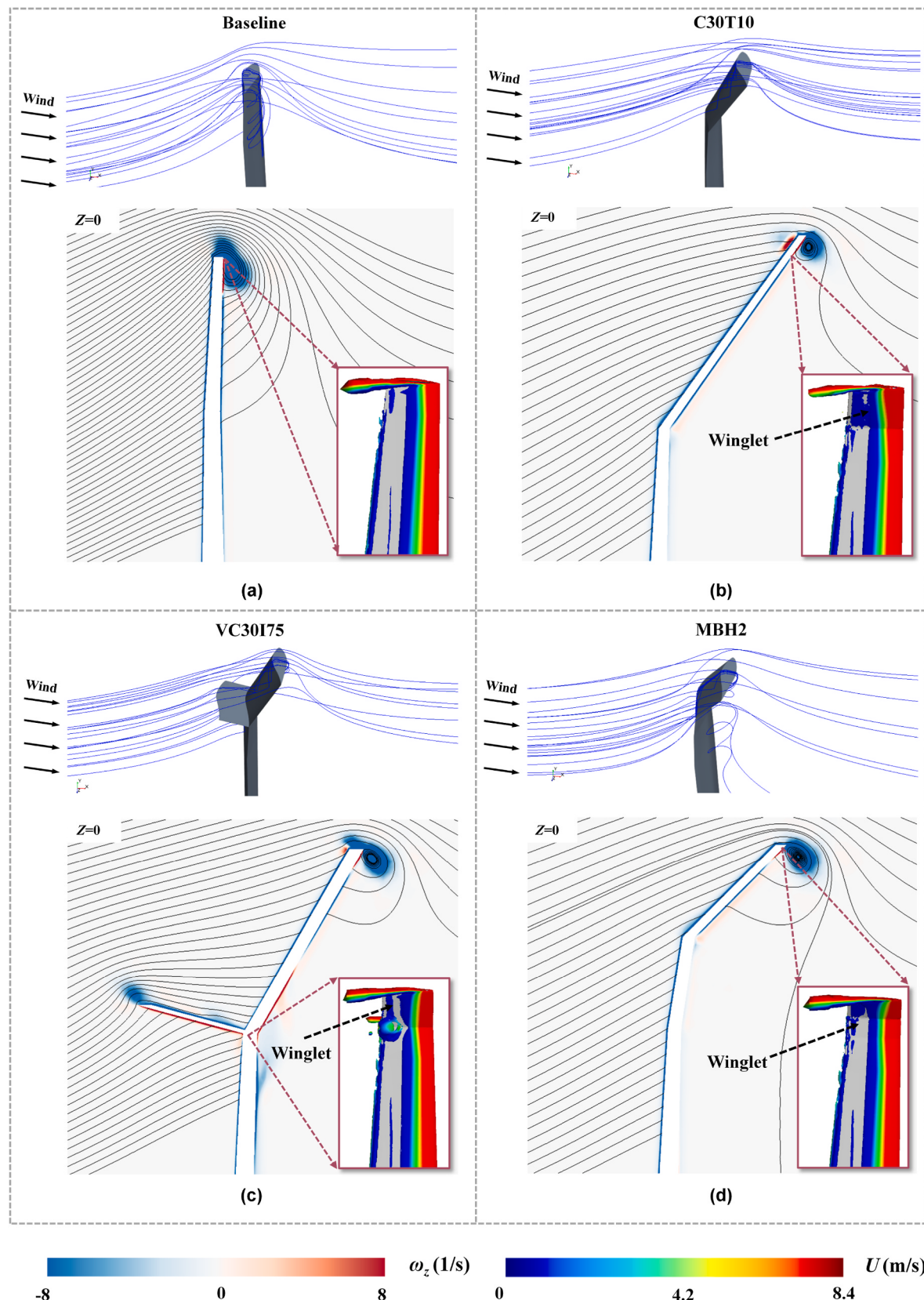


Fig. 16. Comparison of 3-D streamline and vorticity at the blade tip region between baseline blade and 3 configurations of winglets: (a) Baseline; (b) C30T10; (c) VC30I775; (d) MBH2.

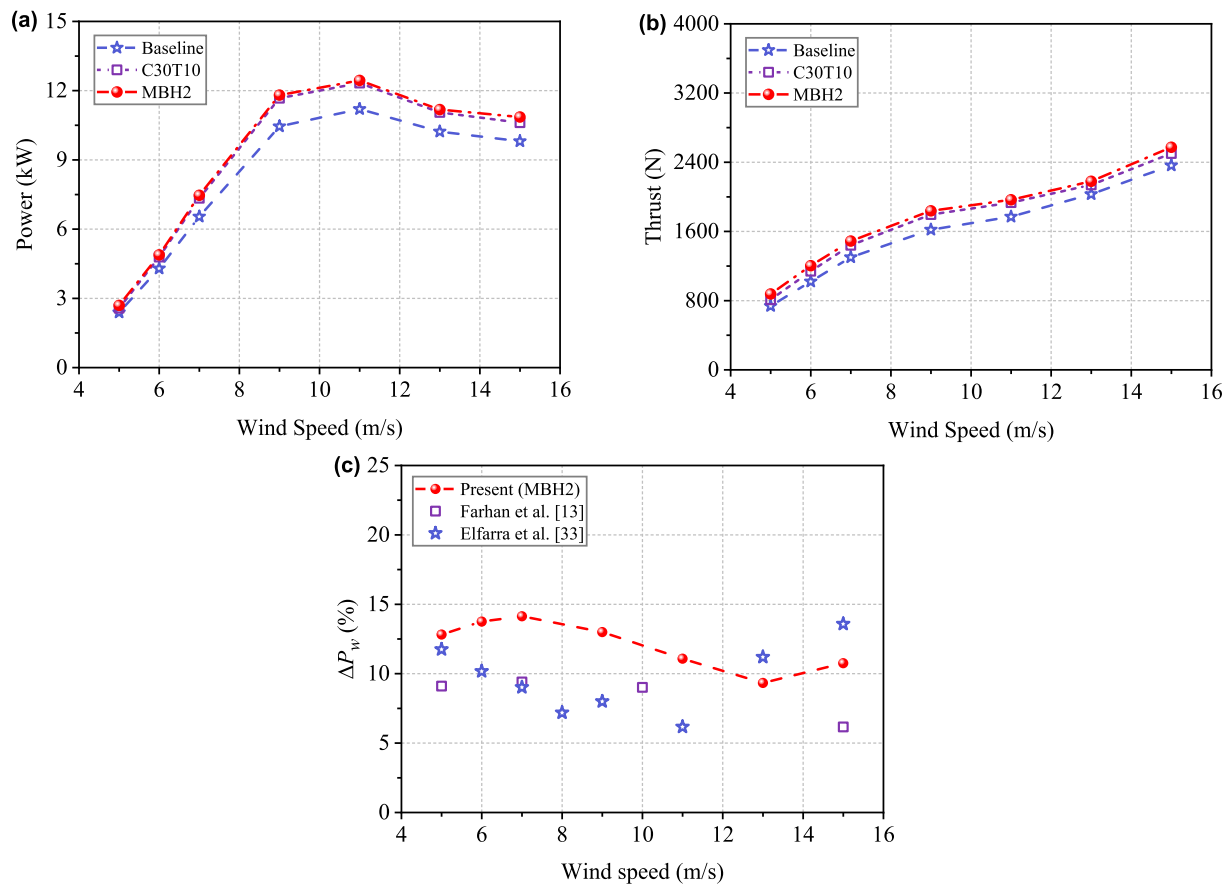


Fig. 17. Comparison of calculated power and thrust using different winglet designs with the baseline at different wind speeds: (a) power; (b) thrust; (c) variation of power gains with wind speed (pentagrams represent the results of Ref. [36], squares indicate the results of the Ref. [16]).

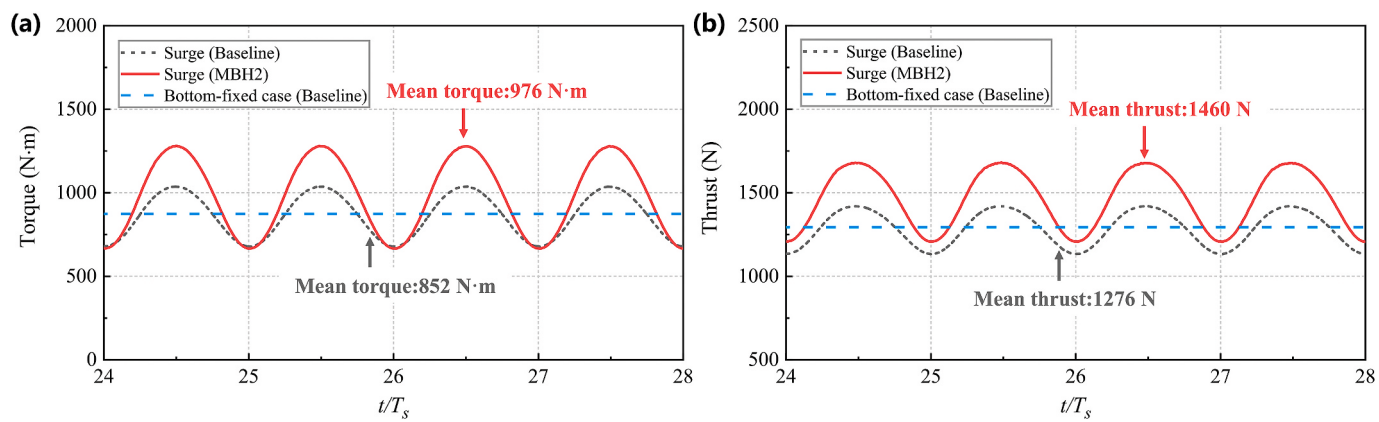


Fig. 18. Comparison of calculated power and thrust using winglet design (MBH2) with the baseline under the surge motion: (a) torque; (b) thrust.

period of the surge motion is conducive to relieving the fatigue of the wind turbine.

5. Conclusion

In the current study, the aerodynamic characteristics of a bent winglet and the basic winglet are compared and studied based on the NREL Phase VI wind turbine using the CFD method. The bent winglet is constructed by bending the middle height of the optimal winglet and the bending parameter is optimized to obtain the best power improvement. The power and thrust gains of the bent winglet have been analyzed at various wind speeds. The study also examines the aerodynamic

characteristics of the bent winglet under platform surge motion. The main findings of the study are as follows:

- (1) The application of the bent winglet (MBH2) can significantly improve the power of HAWT by 14.1%. The MBH2 winglet has better aerodynamic performance than the baseline, resulting in increased energy capture and reduced blade tip loss effect, but it also leads to increased aerodynamic load on the HAWT.
- (2) The pressure coefficient of the MBH2 winglet on the suction side is the largest among the three winglets (C30T10, VC30I75, MBH2). The C_p of C30T10 winglet on the suction side is the smallest due to the influence of the twist angle. The distribution

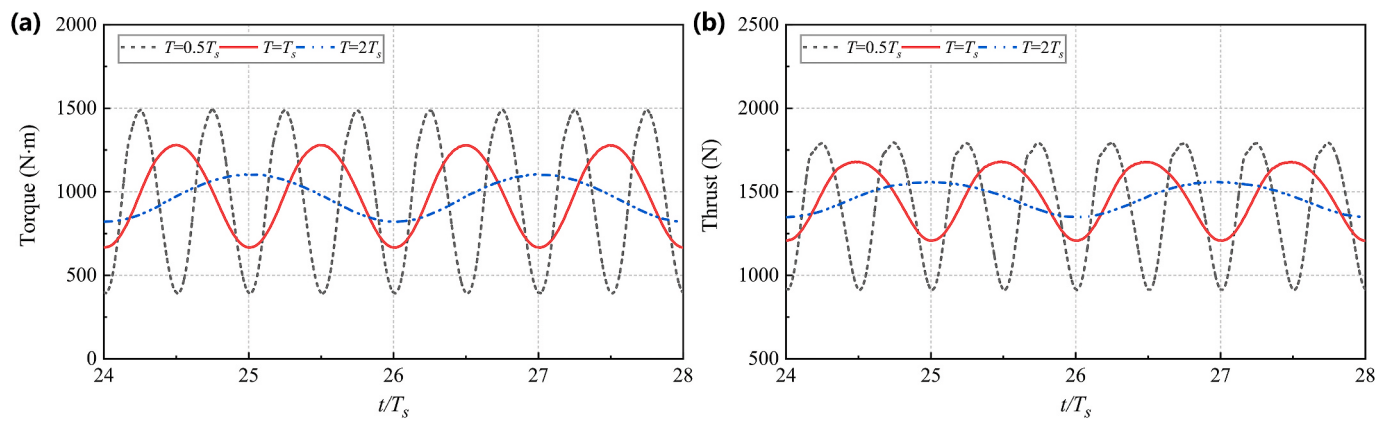


Fig. 19. Comparison of calculated power and thrust under the surge different motion period for the case of MBH2: (a) torque; (b) thrust.

Table 3

Mean, maximum (Max), and standard deviation (Std) of the power and thrust of the wind turbine for the case of MBH2 under three periods of surge motion.

Case	Mean (Torque: N·m/ Thrust: N)	Max (Torque: N·m/ Thrust: N)	Std (Torque: N·m/ Thrust: N)
$T = 0.5T_s$	945/1396	1492/1795	393/315
$T = T_s$	976/1460	1280/1680	217/168
$T = 2T_s$	974/1466	1104/1560	101/75

characteristics of the pressure coefficients of the winglets are related to their aerodynamic performance. The weaker power gain performance of VC30I75 winglet may be due to the effect of the attached tip loss.

(3) The power gain performance of MBH2 winglet is deemed to be the optimal configuration even at different wind speeds. With the action of platform motion, the MBH2 winglet also shows well power performance. Compared to the basic winglet, the proposed new bent winglet can increase the average power output by 14.5% under surge motion. The increase in the surge motion period is conducive to relieving the fatigue of the wind turbine.

Overall, the power gain of above HAWT with winglets is highly limited under various conditions, such as in the limit of standard wind speed of 7 m/s, without considering turbulent inlet, without considering tower structure. Since the current paper includes only a limited number of cant and twist angles, the next work can be done to find the optimal parameters of the bent winglet. The effect of different motions, such as pitch motion, on the aerodynamic performance and wake characteristics of HAWT with bent winglets can likewise be studied.

Credit author statement

Zhihao Zhang, Software, Validation, Writing - Original Draft, Formal

analysis; Limin Kuang, Writing - Review & Editing, Formal analysis; Zhao long Han, Software, Validation, Funding acquisition, Supervision, Writing - Review & Editing; Dai Zhou, Funding acquisition, Review & Editing, Formal analysis; Yongsheng Zhao, Writing - Review & Editing, Formal analysis; Yan Bao, Review & Editing, Formal analysis; Lei Duan, Funding acquisition, Review & Editing, Formal analysis; Jiahuang Tu, Review & Editing, Formal analysis; Yaoran Chen, Funding acquisition, Supervision, Review & Editing; Mingsheng Chen, Funding acquisition, Supervision, Review & Editing.

Declaration of competing interest

The authors declare that they have no known competing financial interests or personal relationships that could have appeared to influence the work reported in this paper.

Data availability

No data was used for the research described in the article.

Acknowledgment

The financial support from the National Natural Science Foundation of China (Nos. 52122110, 52088102, 42076210, 52261043, 52271284, 52171275), Innovation Program of Shanghai Municipal Education Commission (No. 2019-01-07-00-02-E00066), Hunan Provincial Natural Science Foundation of China (2021JJ50027), Hunan Provincial Department of Education Scientific Research Key Project (No. 21A0103), China Scholarship Council (No. 202206230089), The Science and Technology Commission of Shanghai Municipality (No. 22dz1206004), Natural Science Foundation of Shanghai (No. 21ZR1429200) and Oceanic Interdisciplinary Program of Shanghai Jiao Tong University (Nos. SL2021PT302, SL2020PT201 and SL2021PT201) are gratefully acknowledged.

Appendix A. Sensitivity test of the time step

A reasonable selection of the time step is important for predicting the aerodynamics of the HAWT. In this study, a time-step sensitivity test is performed for the selected baseline case. Three-time steps are compared, i.e., $\Delta\theta = 0.5^\circ$, $\Delta\theta = 1^\circ$, and $\Delta\theta = 2^\circ$, as listed in Table A1. It can be seen that the results of $\Delta\theta = 0.5^\circ$, $\Delta\theta = 1^\circ$ and $\Delta\theta = 2^\circ$ are almost identical. Nevertheless, the effect of this small difference on the prediction of aerodynamics can be neglected. Therefore, in consideration of the computational accuracy and efficiency, $\Delta\theta = 1^\circ$ is selected for the rest of the simulations.

Table A1
Comparison of power at different time steps for Phase VI

Case	Time step (°)	Power (kW)
Case 1	0.5	6.50
Case 2	1	6.58
Case 3	2	6.61

Appendix B. Aerodynamic validation under surge motion

To simulate the surge motion, we employed user-defined functions in Star CCM+ that are based on periodic cosine functions and include the period (T_s) and amplitude (A) of the motion. The surge motion function is given by:

$$X_s = A \sin\left(\frac{2\pi}{T_s} t\right) \quad (B1)$$

$$V_s = A \left(\frac{2\pi}{T_s}\right) \cos\left(\frac{2\pi}{T_s} t\right) \quad (B2)$$

where X_s is denoted as the x -axis displacement of the motion of the turbine, and V_s is the matching velocity of surge motion.

The aerodynamics of the surging wind turbine is validated using the NREL 5 MW wind turbine [51] and compared with the data obtained for one cycle of oscillation (shown in Fig. B1). The amplitude of the oscillatory motion is $A = 8$ m and the corresponding period is $T_s = 9.917$ s [52,53]. The data obtained in this study is in good agreement with the literature results and the trend of rotor power and thrust is consistent. Only small deviations are observed at some moments. The numerical model (SST $k-\omega$) used in this study is highly reliable and can accurately simulate the motion of the wind turbine under surge motion.

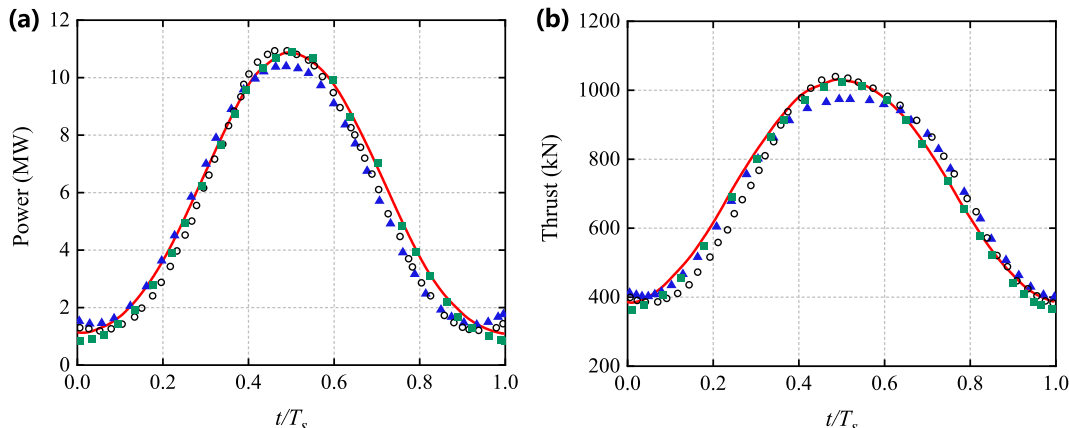


Fig. B1. Comparison of calculated and measured power and thrust using URANS turbulence models under surge motion at $U_\infty = 11.4$ m/s (red lines denote Present; black circles indicate BEM results from the Ref. [53], blue triangles show CFD results from the Ref. [53], boxes represent CFD results from the Ref. [52]): (a) power; (b) thrust

References

- [1] Zeng XM, Shi W, Michailides C, et al. Numerical and experimental investigation of breaking wave forces on a monopile-type offshore wind turbine. *Renew Energy* 2021;175:501–19.
- [2] Zeng XM, Shi W, Feng XY, et al. Investigation of higher-harmonic wave loads and low-frequency resonance response of floating offshore wind turbine under extreme wave groups. *Mar Struct* 2023;89:103401.
- [3] Chen YR, Wang Y, Dong ZK, et al. 2-D regional short-term wind speed forecast based on CNN-LSTM deep learning model. *Energy Convers Manag* 2021;244: 114451.
- [4] Musial W, Spitsen P, Duffy P, et al. Offshore wind market report: 2022 edition. Golden, CO (United States): National Renewable Energy Lab. (NREL); 2022. No. NREL/TP-5000-83544.
- [5] Silva de Souza CE, Bachynski-Polić EE. Design, structural modeling, control, and performance of 20 MW spar floating wind turbines. *Mar Struct* 2022;84:103182.
- [6] Korparatsak N, Leephakpreeda T. Analysis and optimal design of wind boosters for Vertical Axis Wind Turbines at low wind speed. *J Wind Eng Ind Aerod* 2016; 159:9–18.
- [7] Stavrakakis G, Kariniotakis G. A general simulation algorithm for the accurate assessment of isolated diesel-wind turbines systems interaction. a general multimachine power system model. *Energy Conversion IEEE Transactions on* 2017; 10(3):577–83.
- [8] Friis-Møller M, Pedersen MM, Larsen TJ. Response analysis of Poseidon P-37—an offshore platform mounted with wave absorbers and wind turbines. 2018.
- [9] Seifi SMS, Mojaddam M, Hashemi Tari P. Optimal design of a blade of a small horizontal axis wind turbine (hawt) with considering mechanical constraints. *Modares Mechanical Engineering* 2018;18(5):405–13.
- [10] Shirzadeh K, Hangan H, Crawford C, et al. Investigating the loads and performance of a model horizontal axis wind turbine under reproducible IEC extreme operational conditions. *Wind Energy Science* 2021;6:477–89.
- [11] Ke WL, Hashem I, Zhang WW, et al. Influence of leading-edge tubercles on the aerodynamic performance of a horizontal-axis wind turbine: a numerical study. *Energy* 2022;239:122186.
- [12] Jain S, Sitaram N, Krishnaswamy S. Computational investigations on the effects of Gurney flap on airfoil aerodynamics. *Int. Sch. Res* 2015;1–11.
- [13] Vuddagiri A, Halder P, Samad A, et al. Flow analysis of airfoil having different cavities on its suction surface. *Prog Comput Fluid Dynam Int J* 2016;16(2):67–77.
- [14] Genç MS, Koca K, Demir H, et al. Traditional and new types of passive flow control techniques to pave the way for high maneuverability and low structural weight for UAVs and MAVs. *Autonomous Vehicles* 2020:131–60.
- [15] Kuang LM, Su J, Chen YR, et al. Wind-capture-accelerate device for performance improvement of vertical-axis wind turbines: external diffuser system. *Energy* 2022; 239:122196.
- [16] Farhan A, Hassanpour A, Burns A, et al. Numerical study of effect of winglet planform and airfoil on a horizontal axis wind turbine performance. *Renew Energy* 2019;131:1255–73.

- [17] Battisti L, Zanne L, Dell'Anna S, et al. Aerodynamic measurements on a vertical axis wind turbine in a large scale wind tunnel. *J Energy Resour Technol* 2011;133(3):031201.
- [18] Amato F, Bedon G, Castelli MR, et al. Numerical analysis of the influence of tip devices on the power coefficient of a VAWT. *International Journal of Aerospace and Mechanical Engineering* 2013;7(6):1053–60.
- [19] Maughmer M, Kunz P. Sailplane winglet design. *Technical Soaring* 1998;22(4):116–23.
- [20] Maughmer MD. Design of winglets for high-performance sailplanes. *J Aircraft* 2003;40(6):1099–106.
- [21] Gertz DP. An evaluation testbed for alternative wind turbine blade tip designs. University of Waterloo; 2011.
- [22] Carcangiu CE. CFD-RANS study of horizontal axis wind turbines. Universita' degli Studi di Cagliari; 2008.
- [23] Chen Y, Su J, Han Z, et al. A shape optimization of φ -shape Darrieus wind turbine under a given range of inlet wind speed. *Renew Energy* 2020;159:286–99.
- [24] Zhang C. Aerodynamic, structural and aero-elasticity modelling of large composite wind turbine blades. Loughborough University; 2013.
- [25] Gupta S. Development of a time-accurate viscous Lagrangian vortex wake model for wind turbine applications. University of Maryland; 2006.
- [26] Miao W, Li C, Yang J, et al. Numerical investigation of the yawed wake and its effects on the downstream wind turbine. *J Renew Sustain Energy* 2016;8(3):033303.
- [27] Ji BF, Zhong KW, Xiong Q, et al. CFD simulations of aerodynamic characteristics for the three-blade NREL Phase VI wind turbine model. *Energy* 2022;249:123670.
- [28] Ahmed Noor A, Netto KJ. Computer aided design and manufacture of a novel vertical axis wind turbine rotor with winglet. *Appl Mech Mater* 2014;607:581–7.
- [29] Santiago L, Manuel T, Omar L. Numerical study of the effect of winglets on the performance of a straight blade darrieus water turbine. *Energies* 2018;11(2):1–24.
- [30] Miao WP, Liu QS, et al. A comprehensive analysis of blade tip for vertical axis wind turbine: aerodynamics and the tip loss effect. *Energy Convers Manag* 2022;253:115140.
- [31] Zhang TT, Elsakka M, Huang W, et al. Winglet design for vertical axis wind turbines based on a design of experiment and CFD approach. *Energy Convers Manag* 2019;195:712–26.
- [32] Narayan G, John B. Effect of winglets induced tip vortex structure on the performance of subsonic wings. *Aero Sci Technol* 2016;58:328–40.
- [33] Zhu B, Sun XJ, Wang Y, et al. Performance characteristics of a horizontal axis turbine with fusion winglet. *Energy* 2017;120:431–40.
- [34] Gaunaa M, Johansen J. Determination of the maximum aerodynamic efficiency of wind turbine rotors with winglets. *J Phys Conf* 2007;75:012006.
- [35] Johansen J, Gaunaa M, Sørensen NN. Increased aerodynamic efficiency of wind turbine rotors using winglets. In: 26th AIAA applied aerodynamics conference; 2008. Hawaii: Honolulu.
- [36] Elfarra MA, Sezer-Uzol N, Akmandor IS. NREL VI rotor blade: numerical investigation and winglet design and optimization using CFD. *Wind Energy* 2014;17(4):605–26.
- [37] Abbas A, de Vicente J, Valero E. Aerodynamic technologies to improve aircraft performance. *Aero Sci Technol* 2013;28(1):100–32.
- [38] Guerrero Joel E, Dario Maestro, Alessandro Bottaro. Biomimetic spiroid winglets for lift and drag control. *Comptes Rendus Mecanique* 2012;340(1–2):67–80.
- [39] Brocklehurst A, Beedy J, Barakos G, et al. Experimental and CFD Investigation of helicopter BERP tip aerodynamics. In: Conference on computational and experimental methods. University of Glasgow; 2003.
- [40] Robinson K, Brocklehurst A. BER-IV aerodynamics, performance and flight envelope. In: 34th European rotorcraft forum; 2008. Liverpool.
- [41] Hand M. Unsteady aerodynamics experiment Phase VI: wind tunnel test configurations and available data campaigns. Golden, CO (US): National Renewable Energy Lab.; 2001.
- [42] Mo JO, Choudhary A, Arjomandi M, et al. Large eddy simulation of the wind turbine wake characteristics in the numerical wind tunnel model. *J Wind Eng Ind Aerod* 2013;11:211–24.
- [43] Shimizu Yukimaru, Edmond Ismaili, Yasunari Kamada, et al. Power augmentation of a HAWT by Mie-type tip vanes, considering wind tunnel flow visualisation, blade-aspect ratios and Reynolds number. *Wind Eng* 2003;27(3):183–94.
- [44] Su J, Chen YR, Zhou D, et al. Investigation of spanwise wavy configuration for performance improvement of a vertical Axis wind turbine. China. In: Proceedings of the thirtieth (2020) international ocean and polar engineering conference Shanghai; 2020. p. 11–6. October.
- [45] Wang Z, Zhuang M. Leading-edge serrations for performance improvement on a vertical-axis wind turbine at low tip-speed-ratios. *Appl Energy* 2017;208(15):1184–97.
- [46] Duan L, Sun Q, He Z, et al. Wake topology and energy recovery in floating horizontal-axis wind turbines with harmonic surge motion. *Energy* 2022;260:124907.
- [47] Tran TT, Kim D, Nguyen BH. Aerodynamic interference effect of huge wind turbine blades with periodic surge motions using overset grid-based computational fluid dynamics approach. *The Journal of Solar Energy Engineering-transactions of the ASME* 2015;137(6):061003.
- [48] Fang Y, Li G, Duan L, et al. Effect of surge motion on rotor aerodynamics and wake characteristics of a floating horizontal-axis wind turbine. *Energy* 2021;218:119519.
- [49] Li ZB, Dong G, Yang X. Onset of wake meandering for a floating offshore wind turbine under side-to-side motion. *J Fluid Mech* 2022;934:A29.
- [50] Chen G, Liang XF, Li XB. Modelling of wake dynamics and instabilities of a floating horizontalaxis wind turbine under surge motion. *Energy* 2022;239:122110.
- [51] Jonkman J, Butterfield S, Musial W, Scott G. Definition of a 5-MW reference windturbine for offshore system development. Golden, CO (United States): National Renewable Energy Lab. (NREL); 2009. Technical report.
- [52] Tran TT, Kim DH. A CFD study into the influence of unsteady aerodynamic interference on wind turbine surge motion. *Renew Energy* 2016;90:204–28.
- [53] Wen B, Tian X, Dong X, et al. Influences of surge motion on the power and thrust characteristics of an offshore floating wind turbine. *Energy* 2017;141:2054–68.